Mathematics of Sea Ice and Polar Ecosystems

Organizers and Instructors: Kenneth M. Golden and Jody R. Reimer

Summer School Participants and Report Authors:
Daniela Beckelhymer[1]

Lael Costa[2]   Benjamin Gillen[3]   Abby Hardin-Kohli[4]

Daniel Hallman[4]   August Menchaca[5]   Mpho Nefale[6]

Shivani Prabala[7]   Ian Robinson[8]   Amanda Rowley[9]

Jake Weaver[10]   Lilian Zhu[11]   Rosie Fordham[12]

Gabriella Torres Nothaft[13]   Cy Williston[14]   Emma Weber[15]

June 2025, University of Alaska Fairbanks

[1]University of Minnesota Twin Cities
[2]The Pennsylvania State University
[3]University of Southern California
[4]University of Utah
[5]University of Illinois, Chicago
[6]University of the Witwatersrand
[7]University of Michigan
[8]University of Kentucky
[9]University of Nebraska
[10]University of Kansas
[11]Harvey Mudd College
[12]University of Alaska Fairbanks
[13]Cornell University
[14]University of New Hampshire
[15]University of Delaware

Contents

1 Executive Summary

In this summer school, organized and led by Jody Reimer and Kenneth Golden from the University of Utah, students explored mathematical and computational modeling of polar sea ice and ecosystems. Sea ice is a multiscale composite material structured on length scales ranging from tenths of millimeters to tens of kilometers. From tiny brine inclusions and surface melt ponds of increasing complexity, to ice floes of varying sizes in a seawater host, a principal challenge is how to find sea ice effective properties that are relevant to larger scale models, given data on smaller scale structures. Similarly, the sea ice ecosystem ranges from algae living in the brine inclusions to charismatic megafauna like penguins and polar bears, whose diets depend critically, down the line, on the tiny sea ice extremophiles. The dynamics of sea ice microbial communities are regulated by the physics of the ice microstructure, and, in turn, many of these microbes modify their environment by secreting extracellular polymeric substances. In addition to sea ice and its ecosystems, students considered broader mathematical models, including energy balance models, tipping points, and global circulation models.

Workshop Structure

The school consisted of two lectures and two collaborative sessions daily. Collaborative sessions included worksheets reinforcing theoretical content or programming exercises in Google Colab applying sea ice and climate ideas using R or python.

Presentation Overview

Day	Topic	Speaker	Affiliation
Mon	Welcome & Introductions	Organizers	–
	Changing Arctic Overview	Hajo Eicken	University of Alaska
	Sea Ice Microstructure & Percolation	Kenneth Golden	University of Utah
Tue	Sea Ice Biology Intro	Kyle Dillapaine	University of Alaska
	Ice Algal Blooms	Jody Reimer	University of Utah
Wed	Homogenization I	Kenneth Golden	
	Homogenization II	Daniel Hallman	University of Utah
Thu	Remote Sensing I	Christian Sampson	UCAR
	Remote Sensing II	Christian Sampson	
Fri	Polar Bear Movement I	Jody Reimer	
	Polar Bear Movement II	Jody Reimer	
Mon	Sea Ice Geophysics	Andrew Mahoney	University of Alaska
	Fractals in Sea Ice	Kenneth Golden	
Tue	Spatial Heterogeneity	Jody Reimer	
	Diffusion in Sea Ice	Kenneth Golden	
Wed	Climate Math	Kenneth Golden	
	Ecological Tipping	Abby Hardin-Kohli	University of Utah
Thu	Matrix Population Models	Jody Reimer	
Fri	Final Lecture	TBD	TBD

2 Detailed Lecture Summaries

Intro to a Changing Arctic by Hajo Eicken
Summarized by Daniela Beckelhymer

The Arctic is undergoing rapid environmental shifts with far reaching implications. Hajo Eicken, director of the International Arctic Research Center, presented a systems-focused perspective on what is changing, why it matters, and how we can respond as mathematicians. He noted that global conditions no longer align with earlier expectations for near-term stabilization. In the Arctic, conditions are evolving at roughly three times the rat of other regions which is a trend experts refer to as Arctic amplification. Eicken shared a clear message: limiting environmental warming to 1.5°C is no longer a viable target for the near or midterm future. The Arctic is warming at three time the global rate, this is called Arctic Amplification. The Arctic plays a critical role in stabilizing global systems. It influences ocean currents, weather patters, and water distribution across continents. For examples, shifts in Arctic conditions can redirect storm tracks over the North Atlantic, alter rainfall in the central United States, and impact the reliability of seasonal forecasts. The region also supports key economic sectors. Fishers in the Bering and Barents Seas rely on productive Arctic ecosystems. Shipping companies increasingly navigate high-latitude routes as sea ice thins. Indigenous communities depend on the land and sea for food, culture, and continuity.

Therefore, to reduce risks and support long term planning, Eicken recommended a three part strategy. First, decision makers must identify the full range of benefits Arctic systems provide, from ecosystem productivity and maritime access to natural regulation of global processes. Second, institutions must strengthen collaboration across scientific fields, government agencies, and local communities to address complex challenges. Third, leaders must invest in the tools that enable sound planning: observational systems, simulation models, and data driven research. Eicken highlighted the growing concern around abrupt transitions, which experts describe as tipping points. These shifts can occur when gradual pressures build until the system crosses a threshold and move rapidly into a new state. The Greenland Ice Sheet provides a key example. If ice loss surpasses a certain level, the sheet may enter a long term retreat that would drive persistent sea level rise worldwide. Similar risks emerge from permafrost thaw and sea ice collapse, which can disrupt infrastructure and economic activity throughout the Arctic and beyond.

Scientific concepts clarify the behavior of these systems. Feedback loops, for example, describe how one change reinforces another. When the sea ice melts, darker ocean surfaces absorb more heat, which accelerates additional melt (see ice-albedo feedback loop). Hysteresis describes systems that cannot return to their previous state even if initial stressors disappear. Irreversibility refers to long-term transformations, like the loss of glacial mass or collapse of marine ecosystems, that society cannot reverse on useful timescales. Path dependency explain how past choices limit future flexibility. Engineers who built on permafrost decades ago now face high maintenance costs as ground conditions shift unpredictably. These examples show that the Arctic functions as both a bellwether and a driver of boarder changes. Events there can influence trade, infrastructure reliability, geopolitical dynamics, and food systems. Those who plan ahead, by investing in science, mathematics, strengthening partnerships, and integrating evidence into decision making processes, will reduce exposure to

long term disruptions and protect respective interests.

Sea Ice Microstructure and Percolation by Ken Golden
Summarized by August Menchaca

Mathematical models of sea ice range in scale from kilometers to millimeters. It is through the study of both that the modeling of sea ice is conducted.

Macroscopic Modeling

Sea Ice, which covers around 10% of the Earth's surface, acts as the boundary between the ocean and the atmosphere, mediating the exchange of gasses and momentum. It also acts as a shield from incoming solar radiation. The snow and ice have a very high albedo, or proportion of reflected sunlight to incident sunlight, of almost 1, whereas the albedo of the dark blue sea and melt pond water is very low, absorbing much of the solar heat. For clarity, the equation for albedo α is as follows.

$$\alpha = \frac{\text{reflected sunlight}}{\text{incident sunlight}}$$

There are three governing equations to modeling sea ice at the macroscopic scale: the ice thickness distribution, Newton's second law for momentum, and the heat equation of sea ice and snow. These three equations cover both crucial dynamics of the sea ice: thermal and mechanical. Physically, sea ice can be thought of as fast-moving plate tectonics. The movement of those plates can be modeled using conservation of momentum.

$$\text{Ice Acceleration} = \text{wind stress} + \text{ocean stress} - \text{Coriolis force}$$
$$-\text{sea surface tilet} + \text{internal ice stress}$$

or

$$m\frac{D\mathbf{u}}{Dt} = -mf\mathbf{k} \times \mathbf{u} + \tau_a + \tau_o - mg\nabla H + F_{int}$$

The thickness of sea ice can be modeled by the following.

$$\frac{Dg}{Dt} = -g\nabla \cdot \mathbf{u} + \Psi(g) - \frac{\delta}{\delta h}(\tau g) + \mathcal{L}$$

Where $\mathbf{u}$ is the ice velocity, Ψ is a mechanical redistribution function, and the last two terms are the growth and melting of the ice.

Finally, the heat equation of sea ice and snow is given by:

$$\frac{\delta T}{\delta t} + \mathbf{u}_{br} \cdot \nabla T = \nabla \cdot k(T)\nabla T$$

The factors that go into this can be thought of as the following.

$$\frac{\text{melt}}{\text{freeze}} = \text{Net shortwave} + \text{incoming longwave} + \text{outgoing longwave}$$
$$+\text{sensible} + \text{evaporative} + \text{conduction}$$

Microscopic Modeling

When sea ice forms, it cannot absorb the salt from the water into its structure. As it grows pockets of salt water get trapped inside and those are called brine inclusions.

Global climate models cannot take into account every single brine channel in the world, and they do not have to. The study of brine allows for the homogenization of sea ice as a material. Homogenization is the process of looking at the smaller components of a system and considering them as a single element. For example, ice has a very low conductivity and water has a very high conductivity, so when we look at the conductivity of sea ice we use an effective conductivity somewhere between the two. The ability to homogenize is one of the reasons the study of the microstructure of sea ice is so important.

Due to the presence of these brine channels and pockets, sea ice is a porous medium. The permeability of which is dependent on the temperature. A sample of sea ice at $-15°C$ may not have any path for water to flow from the top to the bottom, whereas a sample at $-5°C$ may.

Fluid permeability can be modeled via Stoke's equations for fluid velocity $\mathbf{v}^\epsilon$, pressure p^ϵ, and force $\mathbf{f}$ for pore space $\mathcal{P}$:

$$\nabla p^\epsilon - \epsilon^2 \eta \Delta \mathbf{v}^\epsilon = \mathbf{f}, x \in \mathcal{P}$$
$$\nabla \cdot \mathbf{v}^\epsilon = 0, x \in \mathcal{P}$$
$$\mathbf{v}^\epsilon = 0, x \in \delta\mathcal{P}$$

where η is the fluid viscosity. Via two-scale expansion we obtain the macroscopic equations for Darcy's law:

$$\mathbf{v} = -\frac{1}{\eta}\mathbf{k}\nabla p$$
$$\nabla \cdot \mathbf{v} = 0$$

Where $\mathbf{k}(x)$ is the effective fluid permeability tensor and x is an element of the domain.

This leads to the understanding that sea ice permeability is effectively an on/off switch. As the brine volume increases it is natural to think that the fluid will flow more and more steadily through the ice, but it doesn't. Below a brine volume fraction of around 5% the sea ice is effectively impermeable, but above 5% it is permeable. This percolation threshold of $\phi_c \approx 5\%$ corresponds to a critical temperature $T_c \approx -5°C$, and a salinity $S \approx 5$ ppt. This is called the rule of fives. Nutrient replenishment in the ice is controlled by the permeability so biological activity turns on and off according to this rule of fives. This leads into percolation theory, the probabilistic theory of connectedness. We can envision a grid with some edges connected and some not connected with probability p. The percolation threshold is a probability p_c that is the smallest p for which there is an infinite open cluster in an infinite lattice. This percolation threshold is .5 in 2-D for any shaped lattice e.g. triangular, hexagonal, square. For sea ice we are interested in

$$\sigma(p) \approx \sigma_0(p - p_c)^t$$

which describes the effective fluid permeability. With the best estimate for t in 3-D being around 2. This is described as bond percolation, there is also site percolation which is a
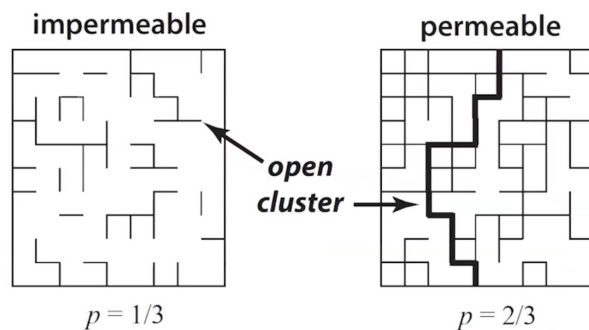
Figure 1: Different lattices with different probabilities of connectedness
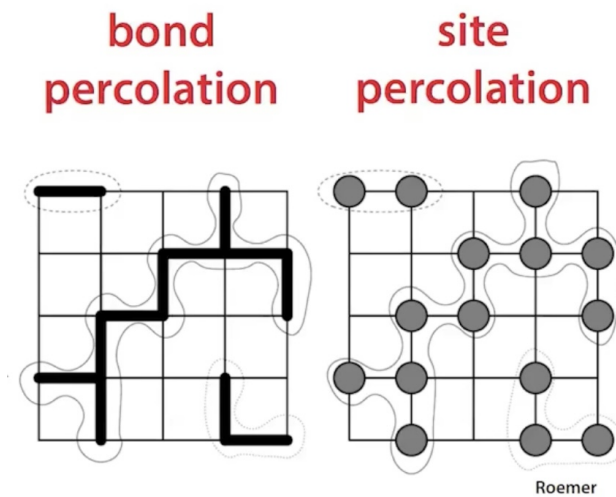

Figure 2: The difference between site and bond percolation

similar problem but instead of the lines of a grid being connected, the squares of a grid are connected. This has a higher percolation threshold in 2-D of $p_c = .59$

Introduction to Life Within Sea Ice by Kyle Dillapaine
Summary by Lilian Zhu and Daniela Beckelhymer

Sea ice is not a sterile barrier; it supports dynamic ecosystems ranging from microbes to small metazoans. Within its porous structure, organisms such as bacteria, archaea, protists, microfauna, and meiofauna have evolved to survive extreme cold, high salinity, and prolonged periods of darkness. The brine channels that form as salt is excluded during freezing create complex networks of microhabitats. These channels experience temperatures from approximately $-1.8°C$ to $-50°C$ and salinities reaching up to 300 parts per thousand, significantly affecting metabolic rates, nutrient transport, and microbial interactions.

Seasonal changes drive the composition and activity of these communities. During the polar night, sea ice ecosystems are largely heterotrophic, with microbial grazers feeding on bacteria and other small organisms. In early spring, increasing sunlight allows photosynthetically active radiation (PAR) to penetrate the thinning ice, enabling blooms of ice-associated algae. Most algal growth occurs within the lower 10 centimeters of the ice, where conditions are more permeable and less saline. Species such as *Fragilariopsis cylindrus* and *Attheya septentrionalis* show different growth patterns in response to these gradients, contributing to ecosystem diversity and function.

To survive these harsh conditions, sea ice organisms exhibit a range of physiological adaptations. Extracellular polymeric substances (EPS) help retain moisture, stabilize temperature and salinity, and create buffered microenvironments within the brine matrix. These EPS can clog brine channels, reducing drainage and slowing the loss of nutrients. Intracellular adaptations such as ice-binding proteins allow organisms to control the formation of ice crystals and protect cellular structures.

The physical permeability of sea ice directly affects the potential for biological activity. Once the temperature rises above approximately $-5°C$, the brine volume reaches a critical threshold of about 5 percent. At this point, the ice becomes permeable enough to allow fluid flow, nutrient exchange, and increased biological interactions. This empirical relationship, often referred to as the "rule of fives" ($-5°C$, 5 percent brine volume, 5 parts per thousand salinity), highlights a key connection between physical and ecological processes in sea ice.

Sampling life within sea ice presents technical challenges. Ice coring is destructive, and the biological material degrades rapidly after extraction. To preserve sample integrity, researchers must work quickly, use osmotic buffers, and apply filtered seawater when measuring biological processes such as photosynthesis. Despite these difficulties, studying sea ice ecosystems is essential. These communities contribute to broader Arctic food webs, influence regional biogeochemical cycles, and serve as sensitive indicators of environmental change. As sea ice thins and melts earlier in the season, the persistence and structure of these ecosystems are likely to shift, with consequences that extend well beyond the Arctic.

Intro to Homogenization

Summarized by Ian Robinson

Composite materials, materials made up of two or more constituent materials, are of great scientific interest. Sea ice is an example of a composite material, being comprised of both ice and brine channels. The essential idea behind homogenization is making use of the small-scale properties of an inhomogeneous material to determine effective (bulk) properties of the larger-scale homogeneous material. In the context of climate, one of our objective is to use the homogenization method to better predict the fate of sea ice and the organisms dwelling within.

Consider passing a curl-free electric field through a square plate Ω, representing a cross-section of sea ice. Then the current density $\mathbf{J}(x)$, satisfying $\nabla \cdot \mathbf{J} = 0$, and the electric field $\mathbf{E}(x)$ are related by the equation

$$\mathbf{J}(x) = \sigma(x)\mathbf{E}(x),$$

where $\sigma(x)$ is the electrical conductivity. Assuming that the ice sample is comprised of both ice and brine channels, we write

$$\sigma(x) = \sigma_1\chi_1(x) + \sigma_2\chi_2(x),$$

where

$$\chi_1(x) = \begin{cases} 1, & x \in \text{ice}, \\ 0, & x \in \text{brine channel} \end{cases}$$

and $\chi_2(x) := 1 - \chi_1(x)$. Now let us denote the average of a function f on Ω by

$$\langle f \rangle := \frac{1}{|\Omega|}\int_\Omega f(x)dx.$$

The goal of homogenization in this scenario is to determine the *effective conductivity* σ^* of the ice sample, where σ^* is defined such that

$$\langle \mathbf{J} \rangle = \sigma^*\langle \mathbf{E} \rangle.$$

From a different point of view, this is the same as seeking a homogeneous medium with electrical conductivity σ^* that behaves the same as the inhomogeneous medium with electrical conductivity $\sigma(x)$. This then separates the problem into two different scales: a local, "zoomed-in" scale at which $\mathbf{J}(x) = \sigma(x)\mathbf{E}(x)$, and a global, "zoomed-out" scale where $\langle \mathbf{J} \rangle = \sigma^*\langle \mathbf{E} \rangle$. The method of homogenization has also been used in many other contexts, including in the study of multi-composite crystals and osteoporotic bone.

Of mathematical interest is determining bounds on the effective properties of a homogenized medium. Using the previous example and considering the field $\mathbf{E} = \mathbf{e_j}$, one may obtain the arithmetic mean bound $\sigma^* \leq \langle \sigma \rangle$. Similarly, in the case $J = e_k$, one may obtain the harmonic mean bound $1/\sigma^* \leq \langle 1/\sigma^* \rangle$. In a more general setting, such bounds are useful for determining regions within which $\Re(\sigma^*)$ and $\Im(\sigma^*)$ must lie for a given sea ice sample, and much work has been devoted to refining these regions.

While the above describes the process of deducing bulk (effective) properties of a material from the local properties, is is also an active area of study to consider the reverse process, which is known as an inverse problem. For example, consider the same ice sample set-up as above, but with the parameter ϵ^* representing the effective permittivity of the homogenized sea ice sample. Then ϵ^* satisfies

$$\langle \mathbf{D} \rangle = \epsilon^* \langle \mathbf{E} \rangle,$$

where $\mathbf{D}$ is the electric displacement field. There exists a Stieltjes integral representation

$$F(s) := 1 - \frac{\epsilon^*}{\epsilon_2} = \int_0^1 \frac{d\mu(z)}{s - z},$$

where $s = 1 - \dfrac{1}{1 - \epsilon_1/\epsilon_2}$, $\mu(z)$ is the spectral measure of the self-adjoint operator

$$-\Gamma := \nabla(-\Delta)^{-1}\nabla \cdot \chi,$$

χ is the characteristic function of the brine phase, and ϵ_1, ϵ_2 are the complex permittivities of the ice and brine, respectively. The inverse problem for this example is then to find $\mu(z)$, which describes the geometry of the inhomogeneous medium, given the bulk complex permittivity ϵ^*. For more information on Stieltjes integral representations and the mathematical treatment of homogenization via the analytic continuation method, see the next section.

Homogenization and the Analytic Continuation Method by Daniel Hallman
Summarized by Ian Robinson

This section serves as a continuation of the previous section on homogenization, which contains definitions necessary for this section. Broadly speaking, the analytic continuation method (ACM) is the mathematical framework for describing homogenization. As in the electrical conductivity example discussed above, one may manipulate Maxwell's equations to find that

$$\chi_1 E = s(sI - \chi_1 \Gamma \chi_1)^{-1} \chi_1 \mathbf{E}_0,$$

where $s = 1 - \dfrac{1}{1 - \sigma_1/\sigma_2}$ and $\mathbf{E}_0 = \langle \mathbf{E} \rangle$. The study of the composite geometry of sea ice (or more general materials) boils down to the analysis of the spectral properties of the operator $\chi_1 \Gamma \chi_1$, which is a self-adjoint projection onto the space of curl-free fields. We denote by $d\mu_{jk}(\lambda)$ a spectral measure of $\chi_1 \Gamma \chi_1$. The above resolvent then leads to a representation for the effective conductivity, given by

$$\sigma_{jk}^* = \sigma_2 \left(\delta_{jk} - \int_0^1 \frac{d\mu_{jk}(\lambda)}{s - \lambda} \right). \tag{1}$$

In practice, the recovery of σ^*, as well as other effective electromagnetic properties, allows one to distinguish between first-year and multi-year sea ice, which is critical for evaluating the health of the polar regions. Distinct physical models, such as the conductivity model

described above, are specific cases of a more generalized ACM framework, with some other specific examples including viscoelasticity, electrical permittivity, advection-diffusion, elastic wave transport, and more. In each of these settings, the effective parameter may be written in a form nearly identical to equation 1, with quantities such as σ_2, s, and the spectral measure appropriately changed to fit the setting.

For one more example, consider the interaction of waves with ice in the marginal ice zone (MIZ), which we may model as a two-phase composite made up of ice floes with viscoelasticity ν_1 and slushy ocean with viscoelasticity ν_2. Quasistatic and incompressibility conditions give rise to the constitutive equations

$$\nabla \cdot \sigma = 0, \quad \epsilon = \epsilon_0 + \nabla^S u, \quad \sigma = 2\nu\epsilon,$$

where σ is the stress tensor, ϵ is the strain tensor, $\nabla^S u$ is the symmetrized gradient applied to the displacement vector, and ν is the viscoelasticity. Then the effective viscoelastic shear coefficient ν^* satisfies $\langle \sigma \rangle = 2\nu^* \langle \epsilon \rangle$, and one may find the resolvent expression for the strain given by

$$\chi_1 \epsilon = s(sI - \chi_1 \Gamma^S \chi_1)^{-1} \chi_1 \epsilon_0,$$

with $s = \dfrac{1}{1 - \nu_1/\nu_2}$, $\Gamma^S = \nabla^S(\nabla \cdot \nabla^S)^{-1}\nabla\cdot$, and $\epsilon_0 = \langle \epsilon \rangle$.

Computationally speaking, direct calculation of the spectral measure allows one to deduce several properties of sea ice, as well as in many other types of media. Using wave data from laboratory and field experiments, one may determine that the effective viscoelasticity follows a quasistatic dispersion relation given by

$$\nu^* = \frac{\rho}{4}\left(\frac{\omega}{k}\right)^2.$$

This allows one to establish rigorous bounds on the effective parameter ν^*, which agree with well known wave-ice datasets.

Data Assimilation and Remote Sensing I by Christian Sampson
Summarized by Jake Weaver and Amanda Rowley

This section began with a broad overview of data assimilation. Namely, we combine a (flawed) model with known data to approximate the true model.

Before getting into DA topics, we took a brief look at why sea ice is important. There are two main reasons, both relating to keeping the earth cool. First of all, sea ice has a large effect on the Earth's albedo, as snow and ice are very reflective. Secondly, sea ice acts as a medium of heat transfer between the atmosphere and the ocean. We noted that the extent of sea ice has been decreasing rapidly in recent years.

We then saw one example of how sea ice is modeled on the large scale, given by the following equation.

$$h\rho\frac{d\nu}{dt} = \nabla \cdot (h\sigma) + t_a + t_w - f_c - \rho h g \nabla H$$

Here, h is the thickness of the ice, ν is the surface drift velocity, ρ is the density of the ice, σ is stress, t_a is atmospheric drag, t_w is oceanic drag, f_c is the Coriolis force, and ∇H is the

sea surface tilt term. The most variable term from model to model is the stress term. In the Community Ice Model (CICE), stress is given by $\sigma_{ij} = 2\eta\dot{\epsilon}_{ij} + (\zeta - \eta)\dot{\epsilon}_{kk}\delta_{ij} - P\delta_{ij}/2$. This model is purely Eulerian, so it is easier to solve, but the cracking of ice is not realistic in this model. In the Material Point Method model, stress is given by $\sigma = \mathbb{E} : (\epsilon - ([[u]] \otimes n)^S\delta_\Gamma)$. This adds a Lagrangian aspect, with jump discontinuities connecting different ice strengths. Lastly in neXtSIM, an Elasto-Brittle Rheology model is used, where we have $\frac{1}{E}\frac{\mathcal{D}\sigma}{\mathcal{D}t} + \frac{1}{\eta}\sigma = K : \dot{\epsilon}$. This is a purely Lagrangian numerical scheme, but DA can be difficult.

To showcase some of the differences, we discussed how MPM is both Lagrangian and Eulerian. Namely, we put a grid down, solve the momentum equation on a Lagrangian time step and track both the nodes and the grid at the same time, and move all of these at once, so we lose no system information. A new grid is placed and the system continues.

On the other hand, neXtSIM does complete non-conservative adaptive meshing, which can simulate sea ice deformation and damage by moving, deleting, and creating grid points.

In addition to the above sea ice models, we must account for ice in the Marginal Ice Zone, an area where sea ice and the open ocean interact. However, in this region, wave-ice interaction becomes crucial to model. In particular, we could consider a two-layer model, where for certain heights, we have a mix of ice and water. However, even with simple assumptions we end up with the equation $\nu = G - i\rho_1\omega v$, which is difficult to determine. That is all to say, our models are complex and flawed, and thus we need Data Assimilation to solve our problems. Thus, we turn to observations instead.

Part 2: Ice Observations One of the most important observations we can make is the concentration of sea ice. The typical way of doing this, at least in the past was using passive microwave sensing, which provides a daily record of sea ice concentration, but typically at a low resolution (14-25km). This is done using brightness-temperature relations. The way to retrieve concentrations from this TB method is by using a bootstrapping algorithm: if one knows the TB of both open ocean and pure sea ice, we may take some tie points, and use this to construct a linear fitting, matching two channels of TB to concentrations of sea ice. However, one downside of this method revolves around the presence of melt ponds. Melt ponds form on the surface of sea ice, but have the same microwave signature as open water. Some ways to get around this involve sticking with summertime tie points, but this can result in underestimation where we have many melt ponds, and overestimation when we are only looking at open water. In addition, wet snow absorbs microwave emissions instead of scattering them, resulting in a different profile as seen by the microwave satellites.

A new method to solve some of these issues is Synthetic Apeture Radar, or SAR. SAR is a remote sensing approach that uses radio frequency waves. It has no need for sunlight, and can be used through any weather conditions. It is versatile as well, as it can collect data at various wavelengths and polarizations, depending on one's purposes. It can penetrate the subsurface, and has a variable resolution as well. These traits make it desirable in many contexts, including those in which it can be used in tandem with other types of data. However, there are some downsides, as the data itself is harder to interpret, and the interaction between the radar signal and the ground can have a great effect, requiring one to be aware of the material and region they are trying to image. For sea ice in particular, salinity, porosity, surface roughness, topography, the presence of layers of snow or water, and the type of snow can all have an impact.

Lastly, as more thoroughly noted in other lectures, the microstructure of sea ice matters

too. One must be aware of the permeability of the ice, and the structure (columnar vs. granular.)

Part 3: Data Assimilation We began with a few Data Assimilation methods. First, for notation, we let x be the state vector, y be the result of applying the observation operator to x, y^o be the observations, x^f be the forecast and x^a be the analysis, H be the observation operator, B be the background error covariance, and R the observation error covariance. We note that both $x - x^f$ and $y - y^o$ are mean zero normal random variables.

For the fully linear case, we have the Kalman Filter, whose equations are

$$x^a = x^f + K(y^o - Hx^f),$$
$$K = BH^T(HBH^T + R)^{-1}.$$

We also have the variational methods, which use a cost function. Examples include 3dVar, given by

$$J(x) = \langle x - x^f, B^{-1}(x - x^f)\rangle + \langle y - y^o, R^{-1}(y - y^o)\rangle$$

and 4dVar, given by

$$J(x) = \langle (x - x^f)B^{-1}(x - x^f)\rangle + \sum_{j=1}^{N}\langle (y_j^o - h(m^j(x))R^{-1}(y_j^o - h(x^j(x)))\rangle.$$

The minimizers for these cost functions are

$$J(\vec{x_0}) = \frac{1}{2}(\vec{x_0} - \vec{x_b})B^{-1}(\vec{x_0} - \vec{x_b}) + \frac{1}{2}[\vec{y}_{t_i} - H_{t_i}M_{0;t_i}(\vec{x_0})]^T R_{t_i}^{-1}[\vec{y}_{t_i} - H_{t_i}M_{0;t_i}(\vec{x_0})]$$

for 3dVar and

$$J(\vec{x_0}) = \frac{1}{2}(\vec{x_0} - \vec{x_b})B^{-1}(\vec{x_0} - \vec{x_b}) + \frac{1}{2}\sum_{i=0}^{N}[\vec{y}_{t_i} - H_{t_i}M_{0;t_i}(\vec{x_0})]^T R_{t_i}^{-1}[\vec{y}_{t_i} - H_{t_i}M_{0;t_i}(\vec{x_0})]$$

for 4dVar.

Of particular note is the presence of Bayesian statistics in these methods. We can use Baye's rule, given by $P(x|y^o) \propto P(y^o|x)P(x)$ to update our distributions, resulting in the above methods. In addition, in the fully linear and Gaussian case, the Kalman Filter and 3dVar work out to be the same.

Lastly, we did a small interactive session in which we intuitively 'derived' the Kalman Filter. Essentially, given some information, our goal was to create sample statistics such as the mean and the variance, and then weight each update by our certainty–essentially the Bayesian update described above.

Polar Bear Movement Models I by Jody Reimer

Summarized by Rosie Fordham

Polar Bears reside within the sea ice covered regions, using the ice for mating and hunting purposes. The loss of sea ice increases the requirement for them to swim, which is five times more energetically costly than walking. The movement of polar bears provides insight into their behaviors that can be used for conservation efforts. Data on Polar movement is gathered using collars placed on adult female Polar Bears, which transmit location information transmitted every two to four hours. This data does not provide a full picture of the movement of the polar bear, and thus mathematical approaches are used to model polar bear movement.

Individual Based Models (IBMs) are used to model this. IBMs represent each individual separately and track their attributes and actions over time. Summary statistics, such as step-length, turn angle, heading, tortuosity and habitual selection, from the IBM path are used to explain and predict polar bear behavior.

A Random Walk (RW) model, which assumes independent movement increments, is a good starting point. In a RW location at time t modeled by

$$\mathbf{x}_{t+1} = \mathbf{x}_t + \boldsymbol{\epsilon}_t, \quad \boldsymbol{\epsilon}_t \sim \mathcal{N}(0, \sigma^2 \mathbf{I})$$

The independence of each step assumed in this model is too simplistic for polar bears, who, we can assume, have some goal driving their movement.

Correlated Random Walks are a natural next step as they capture autocorrelation in movement direction. The location at time t is then modeled using

$$\mathbf{x}_{t+1} = \mathbf{x}_t + l_t \begin{bmatrix} \cos(\phi_t) \\ \sin(\phi_t) \end{bmatrix}, \quad \phi_t = \phi_{t-1} + \theta_t$$

where l_t is the step length, ϕ_t is the heading, and θ_t is the turning angle. Using a Correlated RW improves the model, but still does not capture polar bear movement very well.

Better models can be produced using Resource Selection Functions (RSFs), with the goal of quantifying habitat preference based on environment. This can be achieved by modeling some preference score $\omega(\mathbf{x})$ by the following:

$$\omega(\mathbf{x}) = exp(\beta^\mathsf{T} \mathbf{z}(\mathbf{x}))$$

where $\mathbf{z}(\mathbf{x})$ represents the covariates at location $\mathbf{x}$ and β are the selection coefficients. RSFs compare the "used" locations, those from the actual data, to randomly sampled "available" locations.

Step Selection Functions (SSFs) can be used to create movement informed models. The SSF model below uses logistic regression to compare used vs available steps in a similar way as the RSF model.

$$\omega(\mathbf{x}_t, \mathbf{x}_{t+1}) \propto exp(\beta^\mathsf{T} \mathbf{z}(\mathbf{x}_{t+1} + \gamma^\mathsf{T} \mathbf{m}(\mathbf{x}_t, \mathbf{x}_{t+1})$$

where $\mathbf{z}(\mathbf{x}_{t+1})$ are the habitat covariates at the step endpoint and $\mathbf{m}(\mathbf{x}_t, \mathbf{x}_{t+1})$ are movement features such as step length and turning angle.

Hidden Markov Models (HMMs) additionally explain latent state variables, such as hunting or mating. In HMMs latent state processes are modeled using conditional probabilities;

$$Pr(S_t = j | S_{t-1} = i) = \pi_{ij}$$

and the resulting State-dependent movement model, fit using maximum likelihood or Bayesian models, depends on S_t;

$$f(\mathbf{x}_{t+1} | \mathbf{x}_t, S_t = k) = MovementModel_k$$

In this model each state k governs different movement characteristics.,] HMMs can be combined with SSFs to model state-dependent habitat selection.

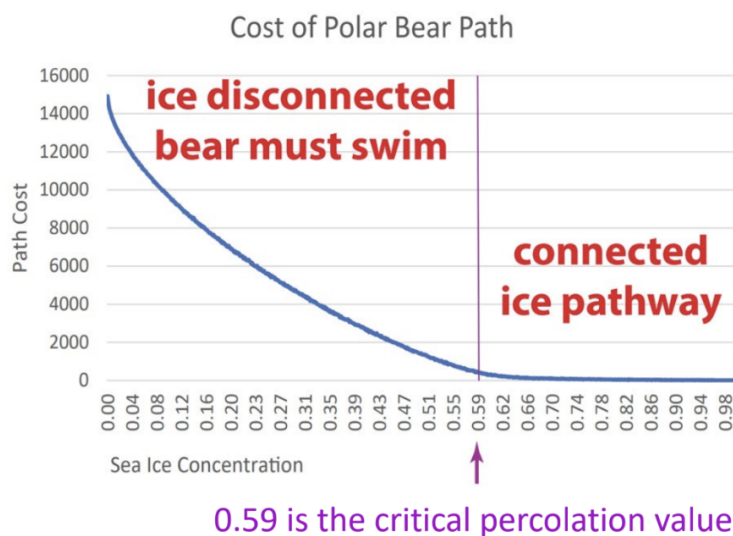## Polar Bear Movement Models II by Jody Reimer
Summarized by Rosie Fordham
This lecture concerned optimal movement for polar bears. Without data on the meso, and micro scale, discerning polar bear movement on small scales requires some inference. It can be assumed that a smart polar bear will make choices that increase their chances for success, success being defined in this context by reproduction and survival. Optimal decision making for polar bear success is modeled in this lecture for three situations; moving through active sea ice, the choice to abandon a reproductive attempt and habitat selection.

Moving through Active Sea Ice
Finding the optimal path through active sea ice, that is sea ice interspersed with open water becomes a percolation problem. In a standard two-dimensional percolation problem the critical percolation value is 0.59. That is, if ice concentration is above 0.59 the polar bear can navigate the ice without having to swim. It is five times more energetically taxing for a polar bear to swim than to walk on ice, so in situations where sea ice concentrations are less than 0.59 it is optimal for polar bears to minimize the amount of time spent swimming in order to conserve energy. The energetic cost of polar bear paths can be modeled using percolation to determine what this optimal path is.

Abandoning a Reproductive Attempt
Female Polar Bears have a built in function that will abandon a pregnancy should she not be fit enough to carry the baby to term safely. This function could depend on the bears body condition, reproductive state and even the environmental conditions.

Habitat Selection
During the winter sea ice period female polar bears must make a choice between active and landfast ice. Active ice provides greater opportunities for hunting seal, but also presents energetic risks due to the need to swim and if the female is with a cub there is the risk that a male polar bear will murder the cub. It is assumed that female polar bears weigh up their need for food with the risks of being in the active ice, mostly in regard

Cost of Polar Bear Path

ice disconnected bear must swim

connected ice pathway

Path Cost

Sea Ice Concentration

0.59 is the critical percolation value

to their cubs. As the ice free period increases polar bears are forced to make riskier choices as their hunting period decreases and the distance they are required to swim to reach active ice increases.
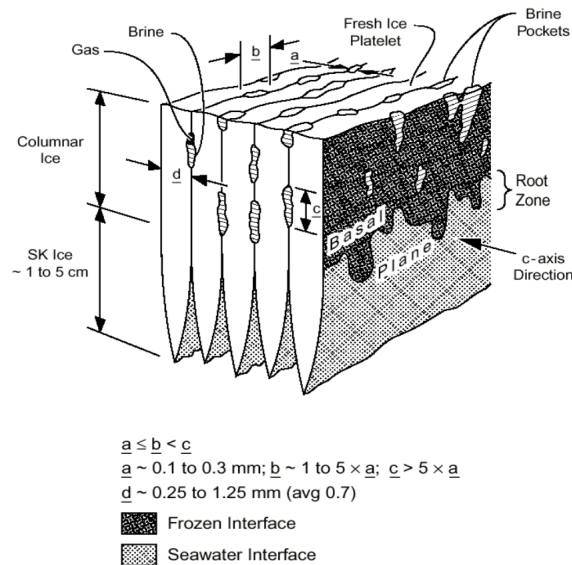
Implications of an Increased Ice Free Period With the ice free period increasing the questions becomes *How does a female polar bear's optimal foraging habitat and optimal reproductive strategy change with the length of the spring feeding season and what are the fitness consequences?* This question is currently being explored using Stochastic Dynamic Programming (SDP). SDP is a state and time dependent approach which includes probabilistic risks and rewards to study optimal tradeoffs. These models contain a time component (t = 0, ..., T), state variables and constraints ($x \in [x_1, ..., x_k]$), possible decisions ($i \in [decisions]$), state dynamics, fitness characterization ($f(x,t)$) and a terminal fitness function ($f(x,T)$). SDP modeling has been used to model the entire lifetime of an adult female polar bear with the goal of maximizing the expected total number of offspring. This included decisions on both habitat and reproduction, and models for the shortening of the spring feeding period due to earlier melts. This modeling found that as ice breakup occurs earlier a female polar bear needs higher energy reserves to continue a reproductive attempt. In addition, if breakup occurs three weeks earlier than the historical date the expected number of offspring decreases from 3.8 to 1.2 cubs per female. With earlier ice breakup this model predicts that females will spend more time in active ice seeking food, and are more likely to abandon a reproductive attempt, leading to fewer successful cubs.

Overview of Sea Ice Geophysics and Remote Sensing by Andrew Mahoney
Summarized by Daniela Beckelhymer

    Andy Mahoney's presentation explored the multifaceted nature of sea ice, emphasizing its geophysical properties and importance across scientific, engineering, ecological, and

cultural domains. Sea ice is not only frozen seawater but it functions as a dynamic component of Earth's climate system and plays a crucial role in shaping life and activity in polar regions. For climatologists, sea ice operates as both a radiator and a water pump in Earths natural cooling system, modulating heat exchange between the ocean and the atmosphere. Ecologists view sea ice as a foundational element of polar ecosystems, providing a platform for primary production and supporting complex food chains, including for marine mammals. To engineers, sea ice presents a design challenge as it is a moving, variable material that serves as a substrate for infrastructure such as ice roads and offshore drilling platforms and a concealment layer for submarines. For indigenous communities, such as the Inupiat, sea ice is integral to daily life: it provides a surface for travel, a source of food and materials, and a deep cultural connection to the Arctic environment.

a ≤ b < c
a ~ 0.1 to 0.3 mm; b ~ 1 to 5 × a; c > 5 × a
d ~ 0.25 to 1.25 mm (avg 0.7)

(Kovacs, 1996)

Glaciologists sea sea ice through a more technical lens, as a crystalline structure formed from seawater, rich in salt and brine inclusions that give it distinct physical and mechanical properties.

Salt plays a vital role in determining the behavior and structure of sea ice. When sea ice forms, only a portion of the salt in seawater become trapped in the ice matrix, typically confined to brine pockets or channels. This entrained brine determines the ice's porosity, permeability, and strength. A key threshold, known as the golden rule, suggests that sea ice becomes permeable when its temperature rises above 5° C and its salinity exceeds 5 parts per thousand, enabling fluid and nutrient transport. These properties are vital for understanding sea ice as a habitat as brine networks support microbial communities and facilitate chemical exchange between the ocean and atmosphere. This has major implications for interpreting radar data. Additionally, the strength of sea ice is significantly lower than that of freshwater ice, being roughly half as strong, due to the brine volume weakening the internal structure. This has important impacts for both engineering safety and modeling ice dynamics.

The formation and melting of sea ice are governed by the surface energy balance which integrates various heat fluxes. These include radiative inputs such as incoming and outgoing solar and thermal radiation, turbulent fluxes from the wind and humidity gradients, and conductive fluxes that move heat through the ice and into the ocean. A simple one dimensional energy balance model can predict whether ice will grow, melt, or warm and is useful for capturing seasonal patterns such as those observed at longterm monitoring sites like Utqiagvik, Alaska.

Surface energy balance of sea ice

$$Q = \left(1-\alpha\right)F_r - I_0 + F_{L\Downarrow} - F_{L\Uparrow} + F_S + F_\ell + F_c$$

Net flux	Absorbed shortwave	Longwave balance	Sensible heat flux	Latent heat flux	Conductive heat flux

Growth, melt or temperature change	=	Radiative fluxes	+	Turbulent fluxes	+	Flux through ice

Mahoney highlights the role of oceanic heat flux at the underside of the ice which can significantly impact basal melt. Sea ice is not stationary. In fact it moves in response to a combination of external and internal forces. The momentum balance equation accounts for wind stress, ocean current drag, the Coriolis effect due to Earth rotation, and internal stress from interactions among ice floes.

Momentum balance of sea ice

$$m\frac{D\boldsymbol{u}}{Dt} = \tau_a + \tau_w + F_i + F_C + F_H$$

Wind stress	Water stress	Internal stress	Coriolis force	Sea surface slope

Total derivative of momentum:

$$\frac{D\boldsymbol{u}}{Dt} = \frac{\partial \boldsymbol{u}}{\partial t} + \boldsymbol{u} \bullet \nabla \boldsymbol{u}$$

inertial forces	momentum advection

When ice concentration is low and floes are isolated, sea ice moves in what is known as free drift, typically $\sim 1\%$ of the wind speed and offset $\sim 5-20°$ to the right due to Coriolis forces. However, in dense pack ice, internal stresses dominate and motion slows, leading to non free drift conditions. Observations over decades show characteristic drift patterns in the Arctic, such as the Beaufort Gyre and Transpolar Drift, both of which are largely driven by geostrophic winds. In fact, roughly 70% of the variability in ice velocity can be explained by these winds alone. The distribution and measurement of sea ice thickness varies significantly by region and age. First-year ice (FYI), which forms and melts within a single season, typically grows up to about 2 meters thick, is highly saline, and provides a suitable environment for ice algae. Multiyear ice (MYI), which survives multiple summers, can reach 5 meters in thickness, has much lower salinity (and is sometimes even drinkable), and provides critical habitat for polar bears, although it supports less biological productivity. Measuring thickness is challenging and can be done through field techniques (like coring and electromagnetic sounding) or remotely using satellite altimetry. Satellite-based methods rely on Archimedes' principle to infer ice thickness from freeboard height—the portion of ice above the waterline—given knowledge of snow depth and ice density.

Seasonal melting reshapes the physical and ecological landscape: FYI typically disappears entirely in summer, while MYI becomes scarred and thinner. Tools like synthetic aperture radar and thermal imaging help differentiate ice types and monitor leads (cracks) and melt ponds from space. These seasonal transformations influence everything from habitat availability to radiative feedbacks in the climate system.

Introduction to Fractals by Ken Golden
Summarized by Lael Costa

The ordinary notion of dimension is a (usually small) integer which allows one to separate objects into several categories ("curve," "surface," "space," etc.) based on how many independent directions of movement they admit. In an imprecise sense, "most" common mathematical objects fall neatly into one of these categories; this lecture concerns those objects which do not.

The term "fractal," a portmanteau of "fractional dimensional," was coined by Benoit Mandelbrot to describe objects which land somewhere between integer dimensions. The tidiest examples are sets of points in Euclidean space which exhibit a direct self-similarity, such as the Sierpiński triangle. This set is constructed inductively by dividing an equilateral triangle into four smaller ones and removing the central one, and then repeating this process with each of the remaining three pieces. Each iteration reduces the area by a quarter, so if the area of the initial triangle is A, then the area of the limiting set is given by

$$\lim_{n \to \infty} \left(\frac{3}{4} \right)^n A = 0.$$

Although the set is embedded in two dimensions, it has no area, and can therefore not really be called 2-dimensional. At the same time, each iteration also increases the length of the boundary of the set by a factor of $3/2$. If the perimeter of the initial triangle is P, then the perimeter of the limiting set is

$$\lim_{n \to \infty} \left(\frac{3}{2} \right)^n P = +\infty.$$

The length of the boundary blows up, and so we also cannot in good conscience say that the Sierpiński triangle is 1-dimensional, either. So what, then is its dimension?

The way forward is to attempt to define dimension through the scaling of "mass" with length. First, consider a square of side length 1 and mass M. If we vary the length scale, we find that mass tracks with length squared: $M(L) \propto L^2$. The two in the exponent corresponds to the fact that the square is 2-dimensional. Repeating this exercise with a line segment or a cube would give that mass grows with the first or third power of length, respectively.

The Sierpiński triangle has the property that it contains three copies of itself, each scaled down by a factor of 2 along each axis. In other words, if we suppose that the mass of a Sierpiński triangle with side length 1 is M, then a Sierpiński triangle with side length 2 must be $3M$. This implies that mass scales with a non-integer power of length:

$$M \propto L^{\log(3)/\log(2)}.$$

The exponent, $\log(3)/\log(2) \approx 1.58$ is declared to be the fractal dimension of the Sierpiński triangle.

Mathematics allows for objects with true self-similarity over all scales. In nature, self-similarity also occurs, although of course only over a limited range of length scales. The crinkled edge of an iris petal, the leaves of ferns, and the florets of Romanesco broccoli each exhibit several iterations of geometrical self-similarity. Porous media such as sandstone do not demonstrate such precise repetition of shape, but nonetheless exemplify *statistical*

self-similarity, meaning that the density of pores of a certain size scales with some power of length.

Statistical fractal structures appear in a least three ways in the study of sea ice:

1. brine channels inside the ice,

2. melt ponds on the surface of the ice, and

3. the ice floes themselves in the marginal ice zone.

Spatial Heterogeneity and Uncertainty Quantification by Jody Reimer

Summarized by Cy Williston

Parameters in ecological models often carry uncertainty arising from measurement error, spatial heterogeneity, model fitting, epistemic uncertainty, and inherent randomness. To account for this, we can treat parameters as random variables representing heterogeneous or uncertain conditions.

We want to understand how these uncertain inputs affect the model output. Local methods, such as computing partial derivatives at some input point, can indicate which parameters influence the output most strongly, but only in a small neighborhood and they miss nonlinear interactions. In contrast, global methods capture the full range of variability and interactions of the inputs. These approaches are more robust for systems with complex dynamics and uncertainty. The methods discussed below are all global methods.

We take the following algal bloom model as an example system.

Algal Bloom Model Equations

$$\frac{dN}{dt} = \underbrace{a}_{\text{input}} - \underbrace{cNP}_{\text{uptake}} - \underbrace{bN}_{\text{loss}}$$

$$\frac{dP}{dt} = \underbrace{fcNP}_{\text{growth}} - \underbrace{dP}_{\text{death}}$$

Here we have uncertainty in the growth rate c and the initial conditions P_0 and N_0. To observe the effects of this uncertainty, we replace these with random variables C, P_0, and N_0.

Methods for Quantifying the Uncertainty

Monte Carlo: This is a sampling-based method. It involves tagging a large number of samples from the probability distributions of each input parameter, running the model for each sample, and estimating output statistics (e.g., mean, variance) based on the ensemble. Monte Carlo is simple to implement but computationally expensive due to the number of required simulations.

Polynomial Chaos: This is a spectral method that represents uncertain model outputs as expansions in a basis of orthogonal polynomials. Instead of sampling, we write the solution as a weighted sum of known basis functions:

$$N(t; C, P_0, N_0) \approx N_V(t; C, P_0, N_0) = \sum_{j=1}^{m} \tilde{N}_j(t)\, \phi_j(C, P_0, N_0),$$

$$P(t; C, P_0, N_0) \approx P_V(t; C, P_0, N_0) = \sum_{j=1}^{m} \tilde{P}_j(t)\, \phi_j(C, P_0, N_0),$$

where $V = \mathrm{span}\{\phi_j\}_{j=1}^{m}$ is a space of orthogonal polynomials, and the coefficients $\tilde{N}_j(t)$, $\tilde{P}_j(t)$ must be computed. The choice of basis polynomials depends on the distribution of (C, P_0, N_0).

One method of computing these coefficients is to substitute the expansion into the model equations. This transforms the original system of two stochastic differential equations into a larger deterministic system of $2m$ ODEs for $\frac{d\tilde{N}_j}{dt}$ and $\frac{d\tilde{P}_j}{dt}$. This approach is accurate but can be algebraically complex and does not guarantee positivity of solutions.

Gaussian Quadrature: Gaussian quadrature is a nonintrusive method for computing the polynomial chaos coefficients $\tilde{N}_j(t)$, $\tilde{P}_j(t)$, meaning it does not require modifying the model equations.

We carefully sample the inputs (C, N_0, P_0) at M deterministic nodes, denoted $\{C, N_0, P_0\}^{(m)}$, where $m = 1, \ldots, M$. These nodes are typically chosen as the roots of the orthogonal polynomials. Then the coefficients are approximated as:

$$\tilde{N}_j(t) := \sum_{m=1}^{M} \omega^{(m)}\, \phi_j(\{C, N_0, P_0\}^{(m)})\, N(t; \{C, N_0, P_0\}^{(m)}),$$

where $\omega^{(m)}$ are quadrature weights selected based on the distribution of (C, N_0, P_0). The same applies for $\tilde{P}_j(t)$.

This method resembles Monte Carlo but converges faster, requires far fewer simulations and—unlike intrusive methods—preserves positivity of outputs.

Once $\tilde{N}_j$ and $\tilde{P}_j$ are computed, we can easily estimate bloom statistics from the surrogate solution N_V, P_V.

Sobol' Indices: Sobol' indices are a variance-based method. They quantify how much of the output variability can be attributed to each input variable and their interactions.

We write $P(t; C, P_0, N_0)$ as a decomposition of orthogonal components:

$$P(t; C, P_0, N_0) = f_0 + f_1(C) + f_2(P_0) + f_3(N_0) + f_4(C, P_0) + f_5(C, N_0) + f_6(P_0, N_0) + f_7(C, P_0, N_0),$$

where each term is orthogonal and corresponds to a distinct contribution to variance.

The total variance of P then decomposes additively:

$$\mathrm{Var}[P] = V_C + V_{P_0} + V_{N_0} + V_{C,P_0} + V_{C,N_0} + V_{P_0,N_0} + V_{C,P_0,N_0}.$$

The first-order Sobol index is defined by:

$$S_i = \frac{V_i}{\text{Var}[P]},$$

measuring the direct contribution of variable i to output variance. The second-order index:

$$S_{i,j} = \frac{V_{i,j}}{\text{Var}[P]}$$

captures the contribution from interactions between inputs i and j.

These indices allow us to rank inputs by importance and identify where uncertainty reduction will have the most impact.

Diffusion and Sea Ice by Ken Golden
Summarized by Shivani Prabala

Brownian Motion & Diffusion Equation

Brownian motion is the random movement of particles in a fluid due to collisions with smaller molecules, driving diffusion as particles spread from high to low concentration. This process links microscopic randomness to macroscopic patterns and is described by the diffusion equation:

$$\frac{\partial u}{\partial t} = D\nabla^2 u$$

Here, $u(x, t)$ is the probability density of a particle at position x and time t, and D is the diffusion coefficient. The solution is:

$$u(x, t) = \frac{1}{\sqrt{4\pi Dt}} e^{-x^2/4Dt}$$

The probability distribution is Gaussian, spreading with time. The mean squared displacement is $\langle X^2(t) \rangle = 2Dt$, while the standard deviation grows as $\langle |X(t)| \rangle = t^{1/2}$, with variance $\sigma^2 = 2Dt$.

Homogenization for Advection-Diffusion

Advection-diffusion models the transport of quantities like temperature or pollutants in fluids. The equation:

$$\frac{\partial u}{\partial t} = D\nabla^2 u - \mathbf{v} \cdot \nabla u$$

includes advection by the velocity field $\mathbf{v}$. Homogenization averages small-scale dynamics, yielding an effective macroscopic model. Small-scale features such as turbulence increase effective diffusivity, D^*. The relationship is:

$$X^2 t \sim 2D^* t$$

Homogenization simplifies the system by averaging small-scale fluctuations, leading to:

$$\frac{\partial \bar{u}}{\partial t} = D^*\nabla^2 \bar{u}$$

where $\bar{u}$ is the homogenized quantity, and the advection term becomes negligible at large scales.

Advection-Enhanced Diffusion

In systems like sea ice, advection influences the diffusion of nutrients, salt, and heat. The advection-diffusion equation for temperature is:

$$\frac{\partial T}{\partial t} + \mathbf{u} \cdot \nabla T = \kappa_0 \nabla^2 T, \quad \nabla \cdot \mathbf{u} = 0$$

Here, $\mathbf{u}$ is the velocity field and κ_0 is the molecular diffusivity. Homogenization simplifies the system, yielding an effective model:

$$\frac{\partial \bar{T}}{\partial t} = \kappa^* \nabla^2 \bar{T}$$

In this model, $\bar{T}$ represents the averaged temperature field, and κ^* is the effective diffusivity, which accounts for both molecular and enhanced diffusion due to small-scale dynamics. This framework is based on the Stieltjes integral representation for effective diffusivity:

$$\kappa^* = \kappa \left(1 + \int_{-\infty}^{\infty} \frac{d\mu(\tau)}{\kappa^2 + \tau^2} \right)$$

Here, $\mu(\tau)$ is a positive definite measure corresponding to the spectral resolution of the self-adjoint operator $i\Gamma H\Gamma$, where H is a stream matrix, $\Gamma := -\nabla(-\Delta)^{-1}\nabla\cdot$, and Δ is the Laplace operator. This approach allows for accurate numerical computations of spectral measures and effective diffusivity, offering a separation of material properties and flow field effects.

Bounds on Convection-Enhanced Thermal Transport

Effective diffusivity κ^* in advection-enhanced diffusion accounts for both molecular diffusion and advection-driven turbulence. The spectral measure $\mu(\tau)$ helps bound the contributions of small-scale dynamics to thermal transport. Using the Stieltjes integral, rigorous bounds for κ^* can be derived, ensuring accurate thermal transport modeling in turbulent flows, especially in complex systems like sea ice. This approach helps predict the upper limits of thermal transport by incorporating enhanced diffusion due to advection and turbulence.

Flow Scale Model of Anomalous Diffusion in Sea Ice Dynamics

A flow-scale model of anomalous diffusion in sea ice dynamics characterizes the displacement of ice floes under the combined influence of diffusion and advection. The mean squared displacement (MSD) is expressed as:

$$\langle |x(t) - x(0) - \langle x(t) - x(0) \rangle|^2 \rangle \sim t^{\alpha},$$

where α is the Hurst exponent, determining the nature of the diffusion process. For $\alpha = 1$, sparse ice packing and an uncorrelated advective field lead to normal diffusive behavior.

When $\alpha < 1$, dense ice packing and crowding dominate the dynamics, causing sub-diffusive behavior with slower displacement. For $\alpha = \frac{5}{4}$, sparse packing with shear-dominated advection results in a higher-than-normal diffusion rate. Lastly, when $\alpha = \frac{5}{3}$, sparse ice with vorticity-dominated advection accelerates diffusion, resulting in super-diffusion. This model helps capture the varying effects of ice pack structure and advective forces on sea ice dynamics, offering insights into how these factors influence transport processes in polar regions.

Mathematics of Climate by Ken Golden
Summarized by Mpho Mendy Nefale

Spheres of the Climate System

Climate is the outcome of interactions among five major *spheres*, each controlling a different part of the planet's heat and mass budgets:

1. **Cryosphere** – land ice, sea-ice, snow, floating ice shelves, and permafrost. These bright surfaces reflect sunlight and steer global circulation via brine rejection and melt-water input.

2. **Biosphere** – every living organism. Exchanges CO_2, CH_4, H_2O, heat, and nutrients with both air and ocean, closing the carbon and nutrient cycles.

3. **Lithosphere** – continents, ocean basins, and mountains. Shapes wind and current pathways; long-term weathering locks up or releases greenhouse gases.

4. **Atmosphere** – a thin, mobile fluid that redistributes heat and moisture. Cloud cover and greenhouse gases determine short-wave reflection and long-wave trapping of radiation.

5. **Hydrosphere** – the global ocean plus surface fresh water. Stores $> 90\%$ of excess heat and powers the deep overturning "conveyor belt" linking polar ice formation to the tropics.

A Minimal Energy-Balance Model (EBM)

To quantify climate behaviour we start with the simplest physically based model: a single, well-mixed "box" that balances absorbed sunlight against infrared cooling.

- Daily–planetary averaging of the solar constant S_0 gives the *insolation per unit area*

$$Q = \frac{S_0}{4}.$$

- With planetary albedo α and Stefan–Boltzmann constant $\sigma = 5.67 \times 10^{-8} \, \mathrm{W\,m^{-2}K^{-4}}$,

$$E_{\mathrm{in}} = (1-\alpha)Q, \qquad E_{\mathrm{out}} = \sigma T^4.$$

- Treating the surface mixed-layer as a lumped heat capacity C yields

$$C\frac{dT}{dt} = (1-\alpha)Q - \sigma T^4. \tag{2}$$

Equation (2) links temperature change directly to radiative gains and losses.

Calibrating the Greenhouse Blanket

Greenhouse gases reduce the planet's infrared cooling efficiency. A simple way to capture this is to introduce an *effective emissivity* $0 < \varepsilon \le 1$:

$$E_{\text{out}} = \varepsilon \, \sigma T^4.$$

- $\varepsilon = 1$: planet radiates like a perfect black body (no greenhouse effect).

- Smaller ε: stronger greenhouse trapping, weaker cooling, warmer surface.

Modern calibration.

With today's global means $\alpha \simeq 0.30$ and $T \simeq 288\,\text{K}$,

$$\varepsilon = \frac{(1-\alpha)Q}{\sigma T^4} \approx 0.61,$$

so the modern atmosphere sheds only $\sim 61\%$ as much infrared energy as an air-less Earth.

Equilibria, Multiple Steady States, and Climate Tipping

Setting $\frac{dT}{dt} = 0$ in the greenhouse-modified EBM gives

$$(1-\alpha)Q = \varepsilon \, \sigma T^4, \qquad T_{\text{eq}} = \left[(1-\alpha)Q/(\varepsilon\sigma) \right]^{1/4}.$$

Because ice and snow are highly reflective, α itself *decreases* as the planet warms. Making α a function of T turns the equilibrium condition into a cubic with three roots:

1. A warm, mostly ice-free climate,

2. A fully frozen "Snowball Earth,"

3. An intermediate unstable point.

The warm and Snowball branches collide in a saddle-node (fold) bifurcation, so gradual forcing changes can trigger an abrupt, irreversible jump—a classic *tipping point* with hysteresis.

Global Climate Models (GCMs)

While EBMs clarify first-order balances, realistic prediction demands the full laws of motion. State-of-the-art GCMs therefore integrate the Navier–Stokes, thermodynamic, radiative-transfer, and chemical continuity equations for atmosphere, ocean, ice, and land on 3-D grids (horizontal resolution ~ 100 km). They

1. capture how uneven solar heating powers winds and currents,

2. must still parameterise sub-grid processes (turbulence, clouds, convection, melt ponds),

3. and currently lack fully coupled dynamic ice-sheet modules—an active frontier in bridging scales.

Why Sea Level Is Rising
Rising sea level is one of the clearest signals of a warming planet.

1. **Melting land ice** – loss from Greenland, Antarctica, and mountain glaciers directly adds water; a complete melt implies ~ 70m of global mean sea-level rise (GMSL).

2. **Thermal expansion** – warmer seawater occupies more volume, explaining roughly 25% of 20th-century GMSL rise and accelerating in the 21st century.

3. **Glacial-isostatic adjustment** – land once depressed by ice sheets is still rebounding (e.g. British Isles rise while fore-bulge regions subside).

4. **Ice–ocean interaction** – warm currents erosively attack ice-shelf fronts, potentially unleashing abrupt retreat; most GCMs do not yet resolve these feedbacks fully, amplifying uncertainty in future GMSL projections.

Ecological Tipping
Summary by Benjamin Gillen

Ecological tipping is defined as a sudden and drastic change in an ecosystem state. A dynamical system tips if it undergoes a sudden transition between alternative stable steady states. There are three main ways for this shift in steady states to occur: noise-induced tipping (N-tipping), bifurcation-induced tipping (B-tipping), and rate-induced tipping (R-tipping).

- Noise-induced tipping occurs when stochasticity is introduced into the system. Natural systems are noisy; however, they also tend to include R-tipping or B-tipping.

- Bifurcation-induced tipping occurs when a critical threshold for a parameter value is reached. However, the analysis is performed on the autonomous (frozen) system.

$$\frac{dx}{dt} = f(x, \lambda)$$

This requirement implies that parameters are changing infinitely slowly. The system remains in a steady state until the critical threshold is reached, at which point the current steady state disappears. The new steady state is then determined. Note that we only consider end time behavior.

- Rate-induced tipping occurs when a critical rate ρ_{crit} for a parameter value is reached. This analysis is done on the non-autonomous system.
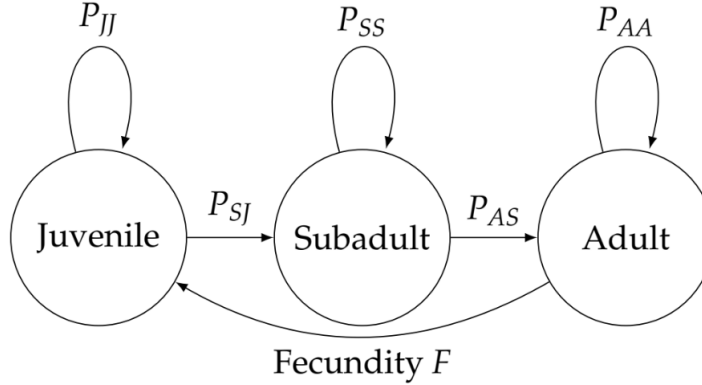
$$\frac{dx}{dt} = f(x, \lambda(\rho t))$$

For some sufficiently large ρ_{crit} that moves towards a different stable steady state, the current state will shift into a new basin of attraction and subsequently converge on that new steady state.

Matrix Models of Polar Marine Mammals by Jody Reimer
Summarized by Rosie Fordham

Matrix population models are used in modeling of polar marine mammals as they allow for tracking of stage-structured populations and forecasting of population size and structure under stochastic or deterministic environments. The summary metrics produced are biologically interpretable and provide a quantitative assessment of management actions.

Projection matrices, which capture the stage-structured population are created from life cycle graphs in a fashion as shown: Work with matrix models such as these began with Leslie

$$\mathbf{A} = \begin{bmatrix} F & F & F \\ P_{SJ} & P_{SS} & 0 \\ 0 & P_{AS} & P_{AA} \end{bmatrix}$$

in 1945, where the matrix $\mathbf{A}$ was defined as follows;

$$A_{ij} = \begin{cases} F_i & \text{if } j = 1 \\ P_{i-1} & \text{if } j = i - 1 \\ 0 & \text{otherwise} \end{cases}$$

This model was expanded upon by Lefkovitch in 1965 to allow for statis and retrogression. From the matrix the dominant eigenvalue $\lambda_1 > 0$ gives asymptotic growth rate of the population. If $\lambda_1 > 1$ then the population grows asymptotically. If $\lambda_1 < 1$ then it declines asymptotically and if $\lambda_1 = 1$ the population is asymptotically stationary. Some biological insight can be gained from the eigenvectors of this matrix, with the right eigenvector giving the stable state distribution while the left eigenvector gives the reproductive value of each stage. Stages with high reproductive value contribute to more long-term growth. The dampening ratio; $\rho = \frac{|\lambda_1|}{|\lambda_2|}$ measures the rate of convergence to stability and can be used in management approaches to target transient amplification or attenuation. Local sensitivity analysis is used in conservation to assess growth rate. Sensitivity of λ to A_{ij} is defined as:

$$s_{ij} = \frac{\partial \lambda}{\partial A_{ij}} = \mathbf{v}_i \mathbf{w}_j$$

Elasticity, or proportional sensitivity, compares contributions from each stage in the matrix and is calculated using:

$$e_{ij} = \frac{a_{ij}}{\lambda} s_{ij}$$

with the elasticities across the matrix summing to 1.

These matrix models can be expanded to account for life expectancy and coupling.
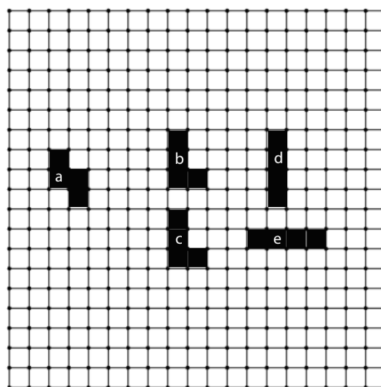
3   Selected Solutions to Collaborative Sessions

Session: Sea Ice Microstructure and Percolation

Solutions by Daniela Beckelhymer

1. Beginning Percolation

For example, Figure 1 shows some lattice animals associated with $N = 4$ sites on the square lattice. Clusters b and c are just translations, so they only count as one lattice animal. Clusters d and e are rotations, so they still count as distinct lattice animals.

Five clusters of size $N = 4$, representing three distinct "lattice animals".

For each of the following lattices (see Figure   ), construct as many lattice animals with $N = 3$, $N = 4$ and $N = 5$ as possible. If you're having fun, keep going to higher N!

For each lattice (square, triangular, hexagonal), lattice animals are connected clusters of N sites, ignoring translations.

- For $N = 3$: On a square lattice, possible animals include:

  - A straight line of 3 sites (horizontal or vertical)
  - An "L" shape (2 sites in one direction, then one turning 90 degrees)

  For triangular lattices, additional diagonal connections are possible, increasing the number of shapes.

- For $N = 4$: Adds configurations such as:

  - A 2-by-2 block
  - A "T" shape
  - A zig-zag pattern

- For $N = 5$: Enumeration becomes more complex. You can build these by adding one site to each $N = 4$ animal in all legal directions that maintain connectedness.

The number of lattice animals increases rapidly with N and depends on lattice type. Higher connectivity (as in the triangular lattice) allows for more configurations.

2. Do Site and Bond Percolation Have the Same Threshold?

They do not.

- For square lattices:

  - Site percolation critical probability: $p_c \approx 0.5927$. This means about 59.27% of the sites must be occupied for a spanning cluster to form.
  - Bond percolation critical probability: $p_c = 0.5$. This means 50% of bonds must be open to expect a spanning cluster.

- Why different? Bond percolation only requires connected edges. Site percolation requires both the site and its neighbors to be occupied. So, site percolation is stricter, and p_c is higher.

Therefore, critical thresholds differ depending on whether percolation is site-based or bond-based.

3. 1D Percolation Results

Goal: Find the probability that a randomly selected site is part of a cluster of size s.

Each cluster of size s in 1D is bracketed by unoccupied sites on both sides. The cluster contains s consecutive occupied sites.

- Probability a site is unoccupied: $1 - p$

- Probability of s consecutive occupied sites: p^s

- Total probability of such a cluster: $(1 - p)p^s(1 - p) = (1 - p)^2 p^s$

- This cluster has s sites. So the probability that a *random site* is in such a cluster is:

$$s(1 - p)^2 p^s$$

Cluster Number Frequency $N(s, p; L)$

This counts how many clusters of size s exist on a finite domain of length L.

$$N(s, p; L) = L(1 - p)^2 p^s$$

We are counting total clusters, not probability per site. Each site in L could be the start of a new cluster. That explains the L out front.

Cluster Number Density $n(s, p)$

This removes the finite size effect:

$$n(s, p) = (1 - p)^2 p^s$$

This is the density of clusters of size s in the infinite limit.

Average Cluster Size $\chi(p)$

We define the average cluster size $\chi(p)$ as:

$$\chi(p) = \frac{1}{pL} \sum_{s=1}^{\infty} s^2 N(s, p; L)$$

Substitute $N(s, p; L) = L(1 - p)^2 p^s$:

$$\chi(p) = \frac{1}{pL} \sum_{s=1}^{\infty} s^2 L(1 - p)^2 p^s = \frac{(1 - p)^2}{p} \sum_{s=1}^{\infty} s^2 p^s$$

We need to evaluate:

$$\sum_{s=1}^{\infty} s^2 p^s = \frac{p(1 + p)}{(1 - p)^3}$$

using known power series identities (e.g., calculus techniques).

Now plug back in:

$$\chi(p) = \frac{(1 - p)^2}{p} \cdot \frac{p(1 + p)}{(1 - p)^3} = \frac{1 + p}{1 - p}$$

As $p \to 1$ from below: $\chi(p) \to \infty$. This reflects that clusters grow larger as the system becomes fully occupied.

4. Brine Volume Fraction

Ice at $-3°$C, Salinity 7 ppt

Empirical rule: Brine volume fraction increases with temperature and salinity.

Percolation occurs when:

- Temperature $> -5°$C

- Salinity > 5 ppt

- Brine volume fraction $> 5\%$

Here, $T = -3°C$ and salinity $= 7$ ppt, so all three conditions are met. The ice is permeable.

(2) Columnar Ice, Salinity 8 ppt

We want to find the critical temperature T_c where brine volume fraction reaches 5%.

Higher salinity allows percolation at colder temperatures. Using the brine volume empirical relation:

$$T_c \approx -5.5°C$$

(3) Granular Ice, Salinity 7 ppt

Similar reasoning:

$$T_c \approx -5.2°C$$

These are approximate and based on fitting empirical curves or applying the rule of fives conceptually.

Session: Remote Sensing and Data Assimilation

Link:Google Colab
Solutions by Jake Weaver
The Colab notebooks used for this section are drawn from the Nansen Center. This section
will outline tutorials 8 and 9, which were the two focused on the session.

3.0.1   T8

Exercise: Moment estimation code: Above, we used numpy's (np) functions to compute
the sample-estimated mean and covariance matrix, $\bar{x}$ and $\bar{C}$, from the ensemble matrix
E. Now, instead, implement these estimators yourself: '

$$\bar{x} := \frac{1}{N} \sum_{n=1}^{N} x_n \,, \tag{3}$$

$$\bar{C} := \frac{1}{N-1} \sum_{n=1}^{N} (x_n - \bar{x})(x_n - \bar{x})^T \,. \tag{4}$$

Solution:

```
# Don't use numpy's mean, cov, but rather a 'for' loop.
def estimate_mean_and_cov(E):
    xDim, N = E.shape

    x_bar = np.sum(E, axis=1)/N
    C_bar = np.zeros((xDim, xDim))
    for n in range(N):
        xc = (E[:, n] - x_bar)[:, None] # x_centered
        C_bar += xc @ xc.T
        # C_bar += np.outer(xc, xc)
    C_bar /= (N-1)
    return x_bar, C_bar
x_bar, C_bar = estimate_mean_and_cov(E)
with np.printoptions(precision=1):
    print("Mean =", x_bar)
    print("Covar =", C_bar, sep="\n")
```

Exercise Why do we normalize by (N-1)?
   Solution: In order to produce an unbiased estimator.
   Exc – There's bias, and then there's bias:

1. Note that $1/\bar{C}$ does not appear to be an unbiased estimate of $1/C = 1$. Explain this
   by referring to a well-known property of the expectation, $\mathbb{E}$. In view of this, consider
   the role and utility of "unbiasedness" in estimation.

2. What, roughly, is the dependence of the mean values (vertical lines) on the ensemble
   size? What do they tend to as N goes to 0? What about $+\infty$?

Solution:

1. Visibly, the expected value (mean) of $\frac{1}{C}$ is not 1, so $\frac{1}{C}$ is not unbiased. This is to be expected, since taking the reciprocal is a nonlinear operation.

2. The mean of $\bar{C}$ is 1 for any ensemble size. The mean of $1/\bar{C}$ is infinite for N=2, and decreases monotonically as N increases, tending to 1 as N tends to ∞

Exercise-Vectorization Like Matlab, Python (numpy) is quicker if you "vectorize" loops. This is eminently possible with computations of ensemble moments. Let $X := \begin{bmatrix} x_1 - \bar{x}, & \ldots & x_N - \bar{x} \end{bmatrix}$.

1. Show that $X = E(I - 11^T/N)$, where 1 is the column vector of length N with all elements equal to 1. *Hint: consider column n of X.*

2. Show that $\bar{C} = XX^T/(N-1)$.

3. Code up this, latest, formula for $\bar{C}$ and insert it in

   `estimate_mean_and_cov(E)`

Solution:

1. We note that $E1/N = \bar{x}$, and then $\bar{x} \cdot 1^T = [\bar{x}, \cdots, \bar{x}]$. Thus we have $E - [\bar{x}, \cdots, \bar{x}] = [x_1 - \bar{x}, \cdots, x_N - \bar{x}] = X$ as desired.

2. This follows from the definition of matrix multiplication, as we found $\bar{C}$ by calculating $\frac{1}{N-1} \sum_{n=1}^{N} (x_n - \bar{x})(x_n - \bar{x})^T$, but $x_i - \bar{x}$ is exactly the ith column of X.

3.

```
x_bar = np.sum(E, axis=1, keepdims=True)/N
X     = E - x_bar
C_bar = X @ X.T / (N-1)
```

Exc – Moment estimation code, part 2: Implement the cross-covariance estimator.
Solution:

```
    def estimate_cross_cov(Ex, Ey):
N = Ex.shape[1]
assert N==Ey.shape[1]
X = Ex - np.mean(Ex, axis=1, keepdims=True)
Y = Ey - np.mean(Ey, axis=1, keepdims=True)
CC = X @ Y.T / (N-1)
return CC
```

3.0.2   T9

Exc – Woodbury for the ensemble subspace Write $\bar{K} = X(Y^T R^{-1} Y + (N-1) I_N)^{-1} Y^T R^{-1}$ using the Woodbury identity.

Solution The Woodbury identity states $(H^T R^{-1} H + B^{-1})^{-1} H^T R^{-1} = (BH^T)(R + HBH^T)^{-1}$ for certain matrices. We currently have $\bar{K} = XY^T(YY^T + (N-1)R)^{-1}$. This already looks like the right hand side of the identity, so we make the identifications $B = I_N, H + Y$, and $R = (N-1)R$. Then, we have

$$\bar{K} = X(Y^T(N-1)^{-1} R^{-1} Y + I_N)^{-1} Y^T (N-1)^{-1} R^{-1}.$$

To finish up, factor our the $(N-1)^{-1}$ from under the inverse, which cancels with the other $(N-1)^{-1}$ outside, and leaving a (N_1) on the identity. That is, we have

$$\bar{K} = X(Y^T R^{-1} Y + (N-1) I_N)^{-1} Y^T R^{-1}.$$

The reason we do so is to have a much smaller size matrix inside the inverse calculation.

Exc – KG Workings How does the EnKF reconcile the linear algebra used in the above equation with the fact that the observation operator may be nonlinear?

Solution The observation operator essentially takes samples of the state, and we may perform linear algebra on those. We do all of the relevant calculations using the ensemble statistics, in particular the covariance R.

Exc – Nobias Kalman Update a Show that $\mathbb{E}\bar{x}^a = \bar{x}^f + \bar{K}\{y1^T - H\bar{x}^f\}$.

Solution First note that $\bar{x}^a = \frac{1}{N} E^a 1$ (as E^a holds the analysis, and the 1 adds the columns). Replace E^a with $E^f + \bar{K}\{y1^T - D_{obs} - HE^f\}$, as defined in our update step, to get

$$\bar{x}^a = \frac{1}{N} E^f 1 + \frac{1}{N} \bar{K}(y1^T - D_{obs} - HE^f)1 = \bar{x}^f.$$

To finish up, note that $1^T 1 = N$, and $E^f 1/N = \bar{x}^f$. Lastly, use our assumption that $\mathbb{E}D_{obs}1 = 0$ allows us to conclude that

$$\mathbb{E}\bar{x}^a = \bar{x}^f + \bar{K}\{y1^T - H\bar{x}^f\}.$$

EnKF Nobias b Show that $\bar{P} = [I_D - \bar{K}H]\bar{B}$.

Solution Rewrite the ensemble analysis anomalies X^a as

$$X^a = E^a(I_n - 11^T/N) = (E^f + \bar{K}\{y1^T - D_{obs} - HE^f\}(I_n - 11^T/N).$$

Note that $D = D_{obs} - \bar{r}1^T = D_{obs}(I_N - 11^T/N)$. Make this replacement above to see that

$$X^a = X - \bar{K}D - \bar{K}HE^f(I_N - 11^T/N) = X - \bar{K}(D + HX).$$

We were given that $\bar{B} = (N-1)^{-1}xx^t$ AND $\bar{P} = (N-1)^{-1}X^a X^{aT}$. Replace X^a in $\bar{P}$ to get

$$\bar{P} = (N-1)^{-1}(X - \bar{K}(D + HX))((X - \bar{K}(D + HX))^T.$$

Distribute everything, turn every term with a XX^T into B, and distribute the $(N-1)^{-1}$ to the rest to get

$$\bar{P} = \bar{B} + \bar{K}H\bar{B}H^T\bar{K}^T - \bar{B}H^T\bar{K}^T - \bar{K}H\bar{B}$$
$$- (N-1)^{-1}[XD^T\bar{K}^T + \bar{K}DX^T - \bar{K}DX^TH^T\bar{K}^T - \bar{K}HXD^T\bar{K}^T - \bar{K}DD^T\bar{K}^T].$$

Using the fact that $(N-1)^{-1}DD^T = R$, we can rewrite tha above as

$$\bar{P} = (I_D - \bar{K}H)\bar{B}.$$

Exc: First EnKF
Solution

```
def my_EnKF(N):
"""My implementation of the EnKF."""
### Init ###
E = xa[:, None] + Pa12 @ rnd.randn(xDim, N)
for k in tqdm(range(1, nTime+1)):
    t = k*dt
    ### Forecast ##
    E = Dyn(E, t-dt, dt)
    E += Q12 @ rnd.randn(xDim, N)
    if k % dko == 0:
        ### Analysis ##
        y = obsrvs[[k//dko-1]].T  # current observation
        Eo = Obs(E, t)            # observed ensemble
        # Compute ensemble moments
        Y = Eo - Eo.mean(keepdims=True)
        X = E - E.mean(keepdims=True)
        PH = X @ Y.T / (N-1)
        HPH = Y @ Y.T / (N-1)
        # Compute Kalman Gain
        KG = nla.solve(HPH + R, PH.T).T
        # Generate perturbations
        Perturbs = R12 @ rnd.randn(p, N)
        # Update ensemble with KG
        E += KG @ (y - Eo - Perturbs)
    # Save statistics
    ens_means[k] = np.mean(E, axis=1)
    ens_vrncs[k] = np.var(E, axis=1, ddof=1)
```

Exc: Compute RMSE
Solution

```
rmses = np.sqrt(np.mean((truth - estimates)**2, axis=1))
average = np.mean(rmses)
```

Variations Repeat the experiments with only observing the first component, with having the seed stored, with a small ensemble of 5, and with covariance inflation.

Solution First, change Obs by setting $p = 1$

Next, we insert a command like *seed(i)* in the code. To run the code with a small ensemble, call my_EnKF(5). Lastly, to implement the covariance inflation, add Perturb = D_infl * R_chol @ rnd.randn(p,N). This gives us the following final code:

```
seed(20)
D_infl = 2
    def my_EnKF(N):
"""My implementation of the EnKF."""
### Init ###
E = xa[:, None] + Pa12 @ rnd.randn(xDim, N)
for k in tqdm(range(1, nTime+1)):
    t = k*dt
    ### Forecast ##
    E = Dyn(E, t-dt, dt)
    E += Q12 @ rnd.randn(xDim, N)
    if k % dko == 0:
        ### Analysis ##
        y = obsrvs[[k//dko-1]].T  # current observation
        Eo = Obs(E, t)            # observed ensemble
        # Compute ensemble moments
        Y = Eo - Eo.mean(keepdims=True)
        X = E - E.mean(keepdims=True)
        PH = X @ Y.T / (N-1)
        HPH = Y @ Y.T / (N-1)
        # Compute Kalman Gain
        KG = nla.solve(HPH + R, PH.T).T
        # Generate perturbations
        Perturb = D_infl*R_chol@rnd.randn(p,N)
        # Update ensemble with KG
        E += KG @ (y - Eo - Perturbs)
    # Save statistics
    ens_means[k] = np.mean(E, axis=1)
    ens_vrncs[k] = np.var(E, axis=1, ddof=1)
```

Session: Polar Bear Activity 2

Solutions by August Menchaca
Link:Google Colab

This notebook is split into two sections. The first uses Djikastra's algorithm to see the cost of traversing a graph with two different edge weights. The other section has a few open questions using graphs to model polar bear movements. For the first part all that is required is running the notebook and changing out several key variables where necessary to observe interesting behaviors of the model. Some extensions are listed such as what would happen if there were a cost for the polar bears exiting and entering water as well as different things that could impact the energy of the polar bears. Because this runs of Dijkstra's algorithm and treats this lattice like a graph any alteration could change the path significantly. So it is an open question on what would be the alteration that most resembles polar bears.

Session: Fractal Activity

Solutions by Benjamin Gillen

A complete version of the Fractal worksheet is included in Appendix B.

Figure 3: Iterative construction of the Menger sponge, a three-dimensional generalization of the Cantor set.

Problem 1: Menger Sponge

Let $M(L)$ denote the measure of an object relative to a characteristic length L. The value $M(L)$ is simply a measure of length, area, volume, or mass depending on the context of which dimension we are operating in. If a line of length 1 is scaled by a factor L, then its new measure is L, i.e., $M(1) = 1$ and $M(L) = L$. Similarly, the measure of a unit square satisfies the relation $M(L) = L^2$, and a unit cube satisfies $M(L) = L^3$. In fractal geometry, the power law that an object follows when subject to scaling (over a range of length scales L) determines its fractal dimension, i.e.,

$$M(L) \sim L^{D_f}. \tag{5}$$

Three iterations of the Menger sponge are shown in Figure 3.

(a) Consider the first iteration of the Menger sponge shown in Figure 3. If this were to be shrunk by a factor of 3, how would you be able to construct the second iteration using copies of this smaller, first iteration as building blocks? You can perform this same exercise for the second and third iterations shown in Figure 3 as well.

(b) Suppose that $M(1) = 1$ for the complete Menger sponge. Compute $M(3)$ using the insight from part (a) and express your answer as a power of 3. Since this scaling law holds across all scales L, find D_f in the expression $M(L) = L^{D_f}$.

Answer 1: Menger Sponge

(a) The second iteration of the Menger sponge is built using 20 copies of the first iteration. Clearly, the second iteration is a $3 \times 3 \times 3$ grid of these first iteration sponges, with 7 of the sponges removed. To ensure the second iteration is the same size as the first iteration, we need to shrink these copies to $1/3$ of their original size. To go from the second to the third iteration, we do the exact same process, i.e. we take 20 copies of the second iteration at $1/3$ of their original size.

(b) We have $M(3) = 20$ from part (a). Since this scaling laws holds across all scales, we get that $20 = 3^{D_f}$. Therefore,

$$D_f = \frac{\log(20)}{\log(3)}$$

Problem 2

In fractal porous media, the number of pores with size greater than or equal to λ follows the scaling law

$$N(L \geq \lambda) = \left(\frac{\lambda_{\max}}{\lambda}\right)^{D_f} \tag{6}$$

where $\lambda_{\max}$ is the size of the largest pore. Equation (6) can also be applied to the number of islands on Earth. For a porous material with $\lambda_{\max} = 9$mm and $D_f = 1.7$ compute the following:

(a) Number of pores of size ≥ 3 mm.

(b) Number of pores of size ≥ 1 mm.

(c) What happens as $\lambda \to 0$? Does this make sense for natural fractals or mathematical fractals?

(d) Write the scaling law for the total number of pores for a fractal porous medium.

Answer 2

(a)

$$N(L \geq 3\text{mm}) = \left(\frac{9\text{mm}}{3\text{mm}}\right)^{1.7} \approx 6.47$$

(b)

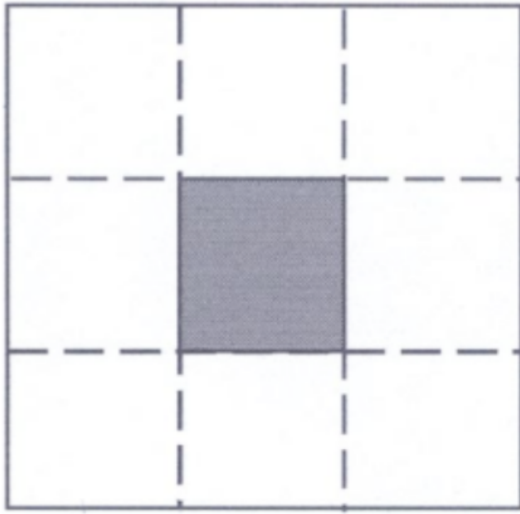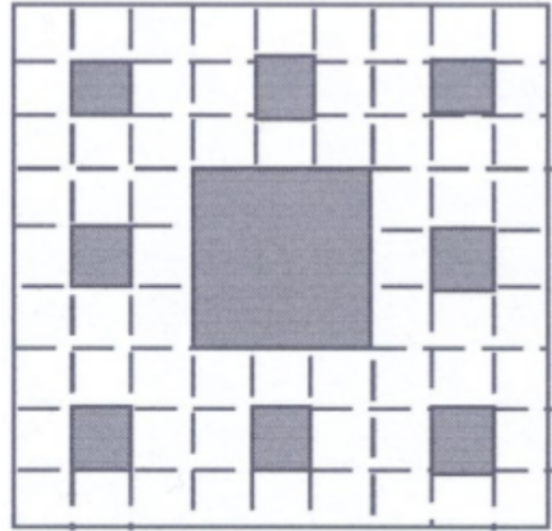$$N(L \geq 1\text{mm}) = \left(\frac{9\text{mm}}{1\text{mm}}\right)^{1.7} \approx 41.90$$

(c) As $\lambda \to 0$,

$$N(L \geq \lambda) = \left(\frac{\lambda_{\max}}{\lambda}\right)^{D_f} \longrightarrow \infty.$$

This divergence makes sense for mathematical fractals as they continue to exhibit structure at arbitrarily small scales (and hence infinitely many pores), whereas natural fractals only follow the scaling law down to some finite lower cutoff.

(d) If the fractal scaling holds only down to a minimum pore size $\lambda_{\min}$, then the total number of pores is

$$N_{\text{total}} = N(L \geq \lambda_{\min}) = \left(\frac{\lambda_{\max}}{\lambda_{\min}}\right)^{D_f}$$

(a) Stage $n = 0$ (b) Stage $n = 1$

Figure 4: Sierpinski carpets of (a) stage $n = 0$ and (b) stage $n = 1$.

Problem 3

We can now draw an interesting connection between the number of pores and the total area of those pores (we are considering a 2D embedding, for simplicity). Consider the zeroth and first iterations of the Sierpinski carpet in Figure 4. Interpreting this as a porous medium, we consider the white squares to be pores and the dark squares to be solid.

(a) Calculate the total area A_t of the porous medium by letting the side length be 3 units (this is specific for Figure 14a). The side length can be considered to be 9 in Figure 14b.

Write your answer as a scaling law similar to Equation (2) and specify what $\lambda_{\max}$ and $\lambda_{\min}$ are. Here, $\lambda_{\max}$ and $\lambda_{\min}$ can be interpreted as the upper and lower limits of self-similar regions, respectively.

(b) Compute the area of pores A_p in Figure 4 and express this as a scaling law similar to part (a), but now with a different scaling exponent. What do you notice about this exponent?

(c) The porosity ϕ can be computed as the ratio A_p/A_t. Write out the scaling law for porosity ϕ, then find an expression for the fractal dimension D_f.

(d) Verify that your equation for D_f works when plugging in suitable values derived from Figure 4.

Answer 3

(a) Clearly, $A_t = 3^2 = 9$. Using our work from the previous question, we see that

$$A_t = \left(\frac{\lambda_{\max}}{\lambda_{\min}}\right)^{D_f}$$

for $\lambda_{\max} = 3$, $\lambda_{\min} = 1$. Since $A_t = 9$, we can conclude that $D_f = 2$.

(b) We now work through the same process, but for only the pores instead of the entire medium. We get that $A_p = 8$ and $8 = 3^{D_f}$. Therefore,

$$D_f = \frac{\log(8)}{\log(3)}$$

(c) Using the scaling law, we can see the porosity is

$$\phi = \frac{(\lambda_{\max}/\lambda_{\min})^{D_f}}{(\lambda_{\max}/\lambda_{\min})^2} = \left(\frac{\lambda_{\max}}{\lambda_{\min}}\right)^{D_f-2}$$

Rearranging,

$$D_f = 2 + \frac{\log(\phi)}{\log(\lambda_{\max}/\lambda_{\min})}$$

(d) We can verify this equation works by plugging in $\phi = 8/9$ and $\lambda_{\max}/\lambda_{\min} = 3$.

$$D_f = 2 + \frac{\log(8/9)}{\log(3)} = 2 + \frac{\log(8) - 2\log(3)}{\log(3)} = \frac{\log(8)}{\log(3)}$$

Session: Diffusion and Sea Ice Worksheet

Solutions by Shivani Prabala

A complete version of the Diffusion and Sea Ice worksheet is included in Appendix B.

Activity #1: Diffusion via random walks

Using a Taylor expansion, show that the Fourier transform of the pdf $f(x)$ is

$$\hat{f}(k) = 1 - (ik)\mu_1 - \frac{k^2}{2}\mu_2 + o(k^2), \tag{7}$$

where, as a reminder, $f(x)$ is the pdf of each of the jumps, Y_i. Using the independence of the jumps Y_i, show that the n-step random walk S_n has Fourier transform $\left(\hat{f}(k)\right)^n$. (**Hint:** an especially "clean" way to do this involves realizing that $\hat{f}(k) = \mathbb{E}[e^{-ikY_i}]$ for each Y_i! You may also need the property that $\mathbb{E}[XY] = \mathbb{E}[X]\mathbb{E}[Y]$ when random variables X and Y are independent. Also note that you never actually need to compute any of the Fourier transforms; an appropriate Taylor expansion is enough!)

Solution:

Given the probability density function (pdf), $f(x)$, of the random jump Y_i, the Fourier transform of $f(x)$, denoted $\hat{f}(k)$, is defined as:

$$\hat{f}(k) = \int_{-\infty}^{\infty} f(x)e^{-ikx}\, dx.$$

We aim to expand this expression using a Taylor series around $k = 0$. First, recall the Taylor expansion of e^{-ikx} around $k = 0$:

$$e^{-ikx} = 1 - ikx - \frac{k^2 x^2}{2} + o(k^2).$$

Substitute this expansion into the definition of $\hat{f}(k)$:

$$\hat{f}(k) = \int_{-\infty}^{\infty} f(x)\left(1 - ikx - \frac{k^2 x^2}{2} + o(k^2)\right)\, dx.$$

We can break this integral into separate parts:

$$\hat{f}(k) = \int_{-\infty}^{\infty} f(x)\, dx - ik \int_{-\infty}^{\infty} x f(x)\, dx - \frac{k^2}{2} \int_{-\infty}^{\infty} x^2 f(x)\, dx + o(k^2).$$

The first term is just the normalization of the probability density function:

$$\int_{-\infty}^{\infty} f(x)\, dx = 1.$$

The second term is the expected value of Y_i, which is denoted by μ_1:

$$\int_{-\infty}^{\infty} x f(x)\, dx = \mu_1.$$

The third term is the expected value of Y_i^2, which is denoted by μ_2:

$$\int_{-\infty}^{\infty} x^2 f(x)\, dx = \mu_2.$$

Thus, the Fourier transform $\hat{f}(k)$ becomes:

$$\hat{f}(k) = 1 - ik\mu_1 - \frac{k^2}{2}\mu_2 + o(k^2).$$

Now, we want to find the Fourier transform of the n-step random walk S_n. Recall that:

$$S_n = \sum_{i=1}^{n} Y_i,$$

where the random variables Y_i are independent and identically distributed (i.i.d.).

We use the fact that the Fourier transform of a sum of independent random variables is the product of their individual Fourier transforms. That is, if $X = Y_1 + Y_2 + \cdots + Y_n$, then:

$$\hat{X}(k) = \hat{Y_1}(k) \cdot \hat{Y_2}(k) \cdots \hat{Y_n}(k).$$

Since the Y_i's are i.i.d., the Fourier transform of each Y_i is the same, i.e., $\hat{f}(k)$. Therefore, the Fourier transform of the sum S_n is:

$$\hat{S_n}(k) = \left(\hat{f}(k)\right)^n.$$

Using a similar argument and supposing (for simplicity) that $\mu_1 = 0$ and $\mu_2 = 2$, show that the normalized sum $\frac{S_n}{\sqrt{n}}$ has Fourier transform

$$\left(\hat{f}\left(\frac{k}{\sqrt{n}}\right)\right)^n = \left(1 - \frac{k^2}{n} + o(n^{-1})\right)^n.$$

In the limit as $n \to \infty$, the above Fourier transform becomes one of our very best friends (mathematically)! How do you evaluate this limit?

Solution:

We use the property that for any random variable X, the Fourier transform of a scaled version aX is:

$$\hat{f_{aX}} = \hat{f}(aX)$$

For the normalized sum $\frac{S_n}{\sqrt{n}}$, the Fourier transform is

$$\hat{f}_{\frac{S_n}{\sqrt{n}}} = \mathbf{E}\left[e^{-ik\frac{S_n}{\sqrt{n}}}\right] = \mathbf{E}\left[e^{-i\frac{k}{\sqrt{n}}S_n}\right] = \hat{f}_{S_n}\left(\frac{k}{\sqrt{n}}\right) \tag{8}$$

From the previous result:
$$\hat{f}_{S_n}(k) = (\hat{f}(k))^n \tag{9}$$

Putting the above two together, we get:
$$\hat{f}_{\frac{S_n}{\sqrt{n}}}(k) = \left(\hat{f}\left(\frac{k}{\sqrt{n}}\right)\right)^n$$

Earlier we found that:
$$\hat{f}(k) = 1 - ik\mu_1 - \frac{k^2}{2}\mu_2 + o(k^2)$$

Plugging in $\mu_1 = 0$ and $\mu_2 = 2$:
$$\hat{f}(k) = 1 - k^2 + o(k^2)$$

Then,
$$\hat{f}\left(\frac{k}{\sqrt{n}}\right) = 1 - \left(\frac{k}{\sqrt{n}}\right)^2 + o\left(\frac{1}{n}\right) = 1 - \frac{k^2}{n} + o\left(\frac{1}{n}\right)$$

and
$$\hat{f}_{\frac{S_n}{\sqrt{n}}}(k) = \left(\hat{f}\left(\frac{k}{\sqrt{n}}\right)\right)^n = \left(1 - \frac{k^2}{n} + o\left(\frac{1}{n}\right)\right)^n$$

Take the limit $n \to \infty$:
$$\lim_{n\to\infty}\left(1 - \frac{k^2}{n} + o\left(\frac{1}{n}\right)\right)^n$$

The small o term vanishes in the limit, so we get the standard exponential limit:
$$\lim_{n\to\infty}\left(1 - \frac{k^2}{n} + o\left(\frac{1}{n}\right)\right)^n = \lim_{n\to\infty}\left(1 - \frac{k^2}{n}\right)^n = e^{-k^2}$$

Now consider the *rescaled random walk* where we replace n by ct, where t represents time and c is whatever scaling factor we need. Show that $S_{[ct]}$ has a Fourier transform $e^{-k^2 t}$ using a lightly modified version of the argument made above.

Solution:

Let
$$S_{[ct]} = Y_1 + Y_2 + \cdots + Y_{[ct]}$$

where $[ct]$ denotes the greatest integer less than or equal to ct, the Y_i are i.i.d. jumps with mean $\mu_1 = 0$, and variance $\mu_2 = 2$. We interpret $t \in \mathbb{R}^+$ as a continuous time parameter, and $c > 0$ as a scaling factor controlling how many jumps happen per unit time.

We modify the argument made above by scaling the random walk by $\frac{1}{\sqrt{c}}$ to obtain a nontrivial limiting distribution as $c \to \infty$. This normalization reflects the diffusive spreading of the walk and ensures convergence to a solution of the diffusion equation. We define the rescaled random walk as:
$$X(t) := \frac{S_{[ct]}}{\sqrt{c}}.$$

Then, the Fourier transform of $X(t)$ is:

$$\hat{f}_{X(t)}(k) = \mathbb{E}\left[e^{-ik \cdot \frac{S_{[ct]}}{\sqrt{c}}}\right] = \hat{f}_{S_{[ct]}}\left(\frac{k}{\sqrt{c}}\right).$$

Recall that for a sum of i.i.d. random variables:

$$\hat{f}_{S_n}(k) = \left(\hat{f}(k)\right)^n.$$

So we apply this to get:

$$\hat{f}_{S_{[ct]}}\left(\frac{k}{\sqrt{c}}\right) = \left(\hat{f}\left(\frac{k}{\sqrt{c}}\right)\right)^{[ct]}.$$

Now, we use the Taylor expansion of $\hat{f}(k)$ near $k = 0$:

$$\hat{f}(k) = 1 - k^2 + o(k^2),$$

so

$$\hat{f}\left(\frac{k}{\sqrt{c}}\right) = 1 - \frac{k^2}{c} + o\left(\frac{1}{c}\right).$$

Therefore:

$$\left(1 - \frac{k^2}{c} + o\left(\frac{1}{c}\right)\right)^{[ct]} \approx \left(1 - \frac{k^2}{c}\right)^{ct}, \quad \text{as } c \to \infty.$$

Now, using the standard exponential limit:

$$\lim_{c \to \infty} \left(1 - \frac{k^2}{c}\right)^{ct} = e^{-k^2 t},$$

we conclude:

$$\hat{f}_{X(t)}(k) \longrightarrow e^{-k^2 t} \quad \text{as } c \to \infty.$$

The Fourier transform of the rescaled random walk $S_{[ct]}$, with proper scaling, converges to

$$e^{-k^2 t}.$$

This is the characteristic function of a Gaussian distribution with variance proportional to t, which matches the fundamental solution to the diffusion equation.

Next, argue that $\hat{p}(k, t)$ solves the ODE

$$\frac{d\hat{p}}{dt} = -k^2 \hat{p} = (ik)\hat{p},$$

and that this ODE can be inverted to

$$\frac{\partial p}{\partial t} = \frac{\partial^2 p}{\partial x^2}. \tag{10}$$

This shows that our rescaled random walk, in the long-time (or, equivalently, "many jumps") limit, has a pdf that satisfies a normal distribution. Remarkably, that same pdf satisfies the diffusion equation![1]

Solution:

To compute the inverse Fourier transform of $\hat{p}(k,t) = e^{-k^2 t}$, we evaluate:

$$p(x,t) = \frac{1}{2\pi} \int_{-\infty}^{\infty} e^{-k^2 t} e^{ikx} \, dk. \tag{11}$$

This is a standard Fourier transform pair known from tables (or can be derived directly via contour integration or completing the square). The result is:

$$p(x,t) = \frac{1}{\sqrt{4\pi t}} \exp\left(-\frac{x^2}{4t}\right). \tag{12}$$

Now, we verify that $\hat{p}(k,t)$ satisfies the ODE:

$$\frac{d\hat{p}}{dt} = -k^2 \hat{p}(k,t). \tag{13}$$

Using the Fourier transform property

$$\mathcal{F}\left[\frac{\partial^2 p}{\partial x^2}\right] = -k^2 \hat{p}(k,t), \tag{14}$$

and the fact that time differentiation commutes with the Fourier transform:

$$\mathcal{F}\left[\frac{\partial p}{\partial t}\right] = \frac{d\hat{p}}{dt}, \tag{15}$$

we invert the ODE to obtain the diffusion equation:

$$\frac{\partial p}{\partial t} = \frac{\partial^2 p}{\partial x^2}. \tag{16}$$

Hence, the limiting pdf of the normalized random walk satisfies the diffusion equation.

---

[1]We have brushed any discussion of the domain of solution or the boundary conditions "under the rug"; as an **extra challenge**, consider what sort of domain and "boundary conditions" would be appropriate here so that our solution is preserved. *It may be worth noticing that "boundary conditions" are in quotes here.*

Activity #2: Pipe bounds on the effective permeability

We restrict our consideration of the brine pore space to the much simplified case that all pores are shaped like small, cylindrical pipes arranged in parallel, each having the same radius a. The Stokes equations reduce to

$$
\frac{1}{r}\frac{\partial}{\partial r}\left(r\frac{\partial w}{\partial r}\right) = -1, \quad r < a
$$
$$
w = 0, \quad r = a
$$
$$
w < \infty, \quad r = 0
$$

(17)

after an appropriate change of coordinates. In this geometry, we are only interested in the z-aligned component of the effective permeability tensor, k_{zz}. Solve for w, the z-component of the velocity field, from the above equations. Then argue that the effective permeability of one cylindrical pipe, of the kind described above, is simply the average velocity w through the pipe. Finally, argue that the effective permeability k of a porous medium consisting of ϕ brine fraction and a cylindrical pipe-like microstructure is

$$
k = \frac{\phi a^2}{8}.
$$

(18)

This effective permeability is the so-called *pipe bound* for a specified radius a.

Solution:

We solve for w by first multiplying through by r:

$$
\frac{\partial}{\partial r}\left(r\frac{\partial w}{\partial r}\right) = -r
$$

Integrate to get:

$$
r\frac{\partial w}{\partial r} = -\frac{1}{2}r^2 + C_1
$$

Then we divide through by r and integrate again:

$$
\int \frac{\partial w}{\partial r} = \int -\frac{1}{2}r + \frac{C_1}{r}
$$

$$
w(r) = -\frac{1}{4}r^2 + C_1\ln\left(r\right) + C_2
$$

Apply the boundary conditions:

1. w must be finite at $r = 0$, thus $C_1 = 0$

2. We use the fact that $w(a) = 0$ to solve for C_2

$$w(a) = -\frac{1}{4}a^2 + C_2 = 0 \rightarrow C_2 = \frac{1}{4}a^2$$

Therefore, the velocity profile is:

$$w(r) = \frac{1}{4}(a^2 - r^2)$$

Next, we find the average velocity through the pipe, $\bar{w}$:

$$\bar{w} = \frac{1}{\pi a^2} \int_0^{2\pi} \int_0^a w(r) r \, dr \, d\theta$$

Substitute in $w(r)$:

$$\bar{w} = \frac{2\pi}{\pi a^2} \int_0^a \frac{1}{4}(a^2 - r^2) r \, dr = \frac{2}{a^2} \cdot \frac{1}{4} \int_0^a (a^2 r - r^3) dr = \frac{1}{8}a^2$$

Next, we argue that the effective permeability k of a porous medium consisting of ϕ brine fraction and a cylindrical pipe-like microstructure is

$$k = \frac{\phi a^2}{8}. \tag{19}$$

Darcy's law for flow through a porous medium:

$$\langle u \rangle = -\frac{k}{\mu} \nabla p$$

where $\langle u \rangle$ is the average fluid velocity at the macroscale, and k is the effective permeability. In our simplified case, we assumed:

$$-\frac{1}{\mu} \nabla p = 1 \rightarrow \langle u \rangle = k$$

In our microstructure, the Darcy velocity is the brine volume fraction ϕ times the average pore velocity:

$$\langle u \rangle = \phi \bar{w} = \frac{\phi a^2}{8}$$

Equating the above two expressions for $\langle u \rangle$, we get:

$$k = \frac{\phi a^2}{8}$$

Before proceeding, consider the effect of supposing that all of the randomly-placed brine pores look like small, parallel pipes aligned in the same direction. This scenario is, in some sense, "extreme". Should it lead to an *overestimate* or an *underestimate* of the effective permeability for random porous media where all pore geometries (and orientations) are

allowed? *Debate and discuss as vigorously as you like, but please remember that if you break furniture, we lose our security deposit.*

If, above, you concluded that the "parallel cylinders" provide an overestimate of the effective permeability, consider what pore geometry and orientation might be associated with an underestimate. If, instead, you concluded that the "parallel cylinders" provide an underestimate, then consider what pore geometry and orientation might be associated with an overestimate. This doesn't need to be fully rigorous; a heuristic approach is just fine. *You may also want to be on the lookout for an interesting analogy between these estimates and certain bounds that may arise in the homogenization session for a completely different physical context.*

Solution:

Assuming that all the brine pores are straight, parallel cylinders aligned with the pressure gradient leads to an **overestimate** of the effective permeability. This idealized geometry maximizes flow efficiency by eliminating bends, tortuosity, dead ends, misalignment, and connectivity issues that would normally reduce permeability in real sea ice. On the other hand, brine pores that are modeled as randomly oriented, highly tortuous, or disconnected would provide an **underestimate** on fluid permeability, as these geometries would restrict flow and create inefficient transport pathways.

Activity #3: Advection-enhanced diffusion

$$\frac{\partial \theta}{\partial t} + u(r)\frac{\partial \theta}{\partial x} = \kappa\left(\frac{\partial^2 \theta}{\partial x^2} + \frac{1}{r}\frac{\partial}{\partial r}\left(r\frac{\partial \theta}{\partial r}\right)\right) \tag{20}$$
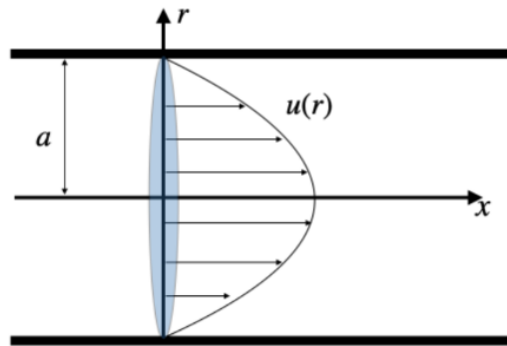

Figure 5: A schematic of shear flow in an axisymmetric pipe.

Consider the *shear flow*,

$$u(r) = 2\bar{u}\left(1 - \frac{r^2}{a^2}\right)$$

where $\bar{u} = \frac{2}{a^2}\int_0^a ur\,dr$. Observe that $\frac{\partial \bar{u}}{\partial r} = 0$; this fact will be useful later.

Now consider the decompositions

$$\begin{aligned}
\theta(x, r, t) &= \bar{\theta}(x, t) + \theta'(x, r, t) \\
u(x, r) &= \bar{u}(x) + u'(x, r),
\end{aligned} \tag{21}$$

where $\bar{\theta} = \frac{2}{a^2}\int_0^a \theta r\,dr$, and $\bar{\theta}' = 0$. *Before proceeding, consider what physical assumptions are being made.*

Apply the above decompositions to Equation (33), simplifying where possible. Take the average of the resulting equation across the radius r and conclude that

$$\partial_t\bar{\theta} + \bar{u}\partial_x\bar{\theta} + \overline{u'\partial_x\theta'} = \kappa\partial_x^2\bar{\theta}. \tag{22}$$

Solution:

Substitute $\theta = \bar{\theta} + \theta'$, and $u = \bar{u} + u'$ into 33:

$$\frac{\partial(\bar{\theta} + \theta')}{\partial t} + (\bar{u} + u')\frac{\partial(\bar{\theta} + \theta')}{\partial x} = \kappa\left(\frac{\partial^2(\bar{\theta} + \theta')}{\partial x^2} + \frac{1}{r}\frac{\partial}{\partial r}\left(r\frac{\partial\theta'}{\partial r}\right)\right)$$

where $\bar{\theta}$ is independent of r, so $\frac{\partial\bar{\theta}}{\partial r} = 0$. Expanding the terms, we get:

$$\frac{\partial\bar{\theta}}{\partial t} + \frac{\partial\theta'}{\partial t} + \bar{u}\frac{\partial\bar{\theta}}{\partial x} + \bar{u}\frac{\partial\theta'}{\partial x} + u'\frac{\partial\bar{\theta}}{\partial x} + u'\frac{\partial\theta'}{\partial x} = \kappa\left(\frac{\partial^2\bar{\theta}}{\partial x^2} + \frac{\partial^2\theta'}{\partial x^2} + \frac{1}{r}\frac{\partial}{\partial r}\left(r\frac{\partial\theta'}{\partial r}\right)\right)$$

Next, we radially average the entire equation. i.e. we apply the radial average operator $\bar{\cdot} = \frac{2}{a^2}\int_0^a(\cdot)r\,dr$ to each term in the above:

$$\frac{\overline{\partial\bar{\theta}}}{\partial t} + \frac{\overline{\partial\theta'}}{\partial t} + \overline{\bar{u}\frac{\partial\bar{\theta}}{\partial x}} + \overline{\bar{u}\frac{\partial\theta'}{\partial x}} + \overline{u'\frac{\partial\bar{\theta}}{\partial x}} + \overline{u'\frac{\partial\theta'}{\partial x}} = \kappa\left(\frac{\overline{\partial^2\bar{\theta}}}{\partial x^2} + \frac{\overline{\partial^2\theta'}}{\partial x^2} + \overline{\frac{1}{r}\frac{\partial}{\partial r}\left(r\frac{\partial\theta'}{\partial r}\right)}\right)$$

We simplify the above term by term:

1. $\frac{\overline{\partial\bar{\theta}}}{\partial t} = \frac{\partial\bar{\theta}}{\partial t}$ (no r dependence)

2. $\frac{\overline{\partial\theta'}}{\partial t} = \frac{\partial}{\partial t}\bar{\theta}' = 0$ ($\bar{\theta}' = 0$)

3. $\overline{\bar{u}\frac{\partial\bar{\theta}}{\partial x}} = \bar{u}\frac{\partial\bar{\theta}}{\partial x}$

4. $\overline{\bar{u}\frac{\partial \theta'}{\partial x}} = \bar{u}\frac{\partial}{\partial x}\bar{\theta}' = 0$

5. $\overline{u'\frac{\partial \bar{\theta}}{\partial x}} = \frac{\partial \bar{\theta}}{\partial x}\bar{u}' = 0$ $(\bar{u}' = 0)$

6. $\overline{u'\frac{\partial \theta'}{\partial x}}$ stays (correlation term)

7. $\overline{\frac{\partial^2 \bar{\theta}}{\partial x^2}} = \frac{\partial^2 \bar{\theta}}{\partial x^2}$

8. $\overline{\frac{\partial^2 \theta'}{\partial x^2}} = \frac{\partial^2}{\partial x^2}\bar{\theta}' = 0$

9. $\overline{\frac{1}{r}\frac{\partial}{\partial r}\left(r\frac{\partial \theta'}{\partial r}\right)} = 0$ (boundary conditions)

We then get:

$$\frac{\partial \bar{\theta}}{\partial t} + \bar{u}\frac{\partial \bar{\theta}}{\partial x} + \overline{u'\frac{\partial \theta'}{\partial x}} = \kappa\frac{\partial^2 \bar{\theta}}{\partial x^2}$$

as desired.

Session: Climate Models

Solutions by Daniela Beckelhymer

Overview of the Climate Energy Balance Model

This worksheet explores a simplified model of the Earth's temperature as it balances incoming solar radiation and outgoing thermal radiation. The fundamental differential equation is:

$$C\frac{dT}{dt} = (1 - \alpha)Q - \epsilon\sigma T^4$$

Parameters

- T: Global average temperature (in Kelvin)

- C: Effective heat capacity of the planet (how much energy is needed to raise the temperature)

- α: Albedo — the fraction of solar radiation reflected by the surface (unitless, between 0 and 1)

- Q: Solar constant (incoming solar energy assuming no reflection), measured in W/m^2

- ϵ: Emissivity — how efficiently the Earth radiates energy (unitless, 0 to 1)

- σ: Stefan-Boltzmann constant (5.67×10^{-8} W/m^2/K^4)

Activity 1: Constant Albedo Model

Set $\frac{dT}{dt} = 0$:

$$T_{\text{eq}} = \left(\frac{(1 - \alpha)Q}{\epsilon\sigma}\right)^{1/4}$$

There is one physical solution for $T_{\text{eq}} > 0$.

Perturb temperature to analyze stability:

$$T(t) = T_{\text{eq}} + \delta T_1(t)$$

Linearizing gives:

$$\frac{dT_1}{dt} = -\frac{4\epsilon\sigma T_{\text{eq}}^3}{C}T_1$$

This implies exponential decay: T_{eq} is stable.

Activity 2: Temperature-Dependent Albedo

We now assume:

$$\alpha(T) = 0.5 - 0.2\tanh\left(\frac{T - 265}{10}\right)$$

Colder temperatures increase albedo due to ice and snow cover, which reflects more light.

This introduces nonlinear feedback into the ODE:

$$\frac{dT}{dt} = (1 - \alpha(T))Q - \epsilon\sigma T^4$$

Now, analytical solutions for T_{eq} are not possible. We use graphical and numerical methods.

Activity 3: Snowball Earth Analysis

We plot $\frac{dT}{dt}$ versus T. Equilibria occur where $\frac{dT}{dt} = 0$ (curve crosses the axis).

Stability Criteria:

- If slope $f'(T) < 0$: stable equilibrium (perturbations decay)

- If slope $f'(T) > 0$: unstable equilibrium (perturbations grow)

Interpretation: Multiple equilibria:

- Cold stable state — "Snowball Earth"

- Middle unstable state — tipping point

- Warm stable state — modern Earth

This simple climate model reveals how nonlinear feedback from albedo can create multiple stable climate states. The Earth can undergo transitions between these states if perturbed beyond critical thresholds, illustrating the importance of tipping points in climate dynamics.

Open Problems in Climate Mathematics at the Poles

Presented by Ken Golden and summarized by Daniela Beckelhymer

Understanding and projecting polar climate dynamics requires a broad mathematical toolkit applied to multiscale, nonlinear, and often data-sparse systems. Below, we outline major open problems and the mathematical approaches needed to address them. These challenges are not only central to advancing polar science, but also to improving global climate projections and understanding life in extreme environments.

1. Multiscale Modeling of the Marginal Ice Zone (MIZ)

Problem: The MIZ is a transitional region between dense pack ice and open ocean. It is a critical zone for atmosphere-ocean-ice interaction and biological productivity.

Mathematical Tools:

- Partial differential equations (PDEs) for phase-change dynamics

- Homogenization theory to derive effective thermal conductivities

- Multiscale modeling frameworks

Importance: Predicting seasonal and decadal shifts in MIZ width and location is essential for climate forecasting, ecosystem modeling, and operational navigation.

2. Filling the Polar Data Gap

Problem: Satellite measurements suffer from data gaps near the poles, leading to incomplete or inaccurate sea ice observations.

Mathematical Tools:

- PDE-based inpainting (e.g., harmonic extension)

- Stochastic models and data assimilation

- Inverse problems for reconstructing missing data

Importance: Accurate ice field reconstructions improve climate records and model validation.

3. Sea Ice as a Composite Material

Problem: Sea ice is a porous, heterogeneous medium with complex thermal and mechanical behavior.

Mathematical Tools:

- Homogenization of composite media

- Effective medium theory

- Fracture mechanics and variational methods

Importance: Constitutive laws derived from these methods are needed for large-scale sea ice models and understanding ice pack dynamics.

4. Modeling Tipping Points and Critical Transitions

Problem: Polar systems can undergo abrupt shifts due to feedback loops (e.g., ice-albedo feedback).
Mathematical Tools:

- Nonlinear dynamical systems

- Bifurcation theory

- Stochastic differential equations (SDEs)

Importance: Identifying early warning signs of tipping points informs climate resilience and risk assessment.

5. Polar Ecosystem Dynamics

Problem: Sea ice supports complex microbial and ecological networks that are sensitive to physical changes.
Mathematical Tools:

- Population dynamics models

- Reaction-diffusion systems

- Network theory for species interactions

Importance: Modeling ecosystem thresholds and resilience under ice loss is key to biodiversity conservation.

6. Machine Learning and Low-Order Models

Problem: High-fidelity models are expensive to run at global scales.
Mathematical Tools:

- Surrogate modeling and emulators

- Reduced-order models

- Physics-informed neural networks (PINNs)

Importance: These tools bridge data and theory, enabling real-time forecasting and uncertainty quantification.

7. Wave–Ice Interactions

Problem: Retreating ice allows waves to penetrate deeper into the pack, increasing breakup and feedbacks.
Mathematical Tools:

- Wave propagation in random media

- Coupled PDE-ODE systems

- Spectral analysis

Importance: Capturing wave-ice feedbacks is critical for predicting MIZ evolution and ice fragmentation.

8. Extraterrestrial Analogs and Astrobiology

Problem: Earth's sea ice systems offer analogs for icy moons and planets.
Mathematical Tools:

- Thermodynamic modeling of brine networks

- Percolation theory

- Stability analysis of life-supporting niches

Importance: Understanding how life adapts in sea ice may inform searches for life beyond Earth.

Summary

Each of these open problems exemplifies how mathematics—particularly PDEs, dynamical systems, homogenization, and machine learning—serves as a foundational tool in understanding polar climate dynamics. Advances in these areas not only deepen our understanding of Earth's climate system, but also offer powerful insights into physics, biology, and planetary science.

4 Mini-Project Reports

4.1 Melt Pond Simulations

Group members: Lael Costa, Safeyya Alyahia, Marco, Jasmine Browne

Motivation: Prof. Golden's lecture on fractals included a discussion of some numerical results concerning the dynamics of melt pond topology and fractal structure. More specifically, one can think of the portion of the ice surface covered by melt ponds as a sub-level set of the ice surface height function, so the topology of the melted volume changes according to Morse theory. Connections are indicated between percolation of the pond network, the Euler characteristic, and the fractal dimension. We wished to further explore these connections, and to repeat the numerical experiments with more complicated surface geometry.

Workup: The simulation is live at `https://lael.dev/sea-ice` (press and hold the space bar to increase the water level; refresh the page to regenerate the ice surface).

Future Directions: A more mechanism-driven model of ice surface geometry would make the results more predictive of real-world behavior. The Euler characteristic computation relies on detection of saddle points in a discrete mesh. This is a non-trivial problem in computational geometry, and the current implementation is, at best, naive. Techniques from discrete differential geometry should be applied to give a more reliable result.

4.2 Tipping in a Plant-Herbivore Model

Group members: Gabriella Torres Nothaft, Shan Gao, Leon Weng, and Joanna Ro

Motivation: One of the additional activities in the Ecological Tipping collaborative session was exploring the tipping behavior of different models. The plant-herbivore model, which showcases a lot of distinct behaviors based on the parameter choices. Interest arose in studying and understanding the tipping points of this system based on parameter functions chosen.

Workup: The plant-herbivore model is defined as:

$$\frac{dP}{dt} = r(t)P - cP^2 - g(P)H$$
$$\frac{dH}{dt} = Ee^{-bP}g(P)H - m(t)H$$
$$g(P) = c_{max}\frac{P^2}{P^2 + a^2}e^{-b_cP}$$

In here, we can see that the growth rate of the plants r and the mortality rate of the herbivore m are both nonautonomous. Also, the functional response $g(P)$ is a modification of the classic type-III response, with a factor e^{-b_cP} to account for herbivores' decreased foraging rates as the amount of biomass increases. A similar factor, e^{-bP}, is also added to the assimilation efficiency of the herbivores, with more biomass leading to decreased quality of biomass.

When looking at the autonomous system, with r and m fixed constants, there are two possible equilibrium states: coexistence or herbivore extinction. When studying the bifurcation diagrams of the autonomous system, we get that the system can undergo either

a transcritical bifurcation or saddle-node bifurcation, depending on the values of b and b_c chosen. When doing a two-parameter autonomous bifurcation diagram, there are multiple bifurcation scenarios that depend on b and b_c, such as Hopf and homoclinic bifurcations, as seen in [1].

For the nonautonomous system, the bifurcations depend on how $r(t)$ and $m(t)$ are defined. For this project, these were set to be Heaviside functions with a 50 time unit delay, of the form:

$$m(t) = m + \Delta_m H(t - 50), \quad r(t) = r + \Delta_r H(t - 50)$$

As Δ_r increases, the system tends towards extinction, with coexistence only occurring for $\Delta_m \ll 1$. The combination of these results shows indications of R-tipping, as intended.

Future Directions: Some possible future directions are studying different forms for the nonautonomous parameters. Additionally, an in-depth analysis of the transitions can elucidate when extinction is reversible. The speed of these transitions can also indicate other types of tipping that are not only rate-induced.

4.3   Homogenization

Group members: Shane, Ed, Cy, Vasilis

Motivation: This mini-project explores a variational approach to bounding effective parameters (such as conductivity or permittivity) in heterogeneous media, following the methods of Golden & Papanicolaou (and others). The goal is to estimate these effective quantities without computing the full homogenized solution, which is often analytically intractable due to the complexity and randomness of the material's microstructure.

Workup: Let $(\Omega, \mathcal{F}, P)$ be a probability space representing random configurations of the microstructure. The problem is framed in terms of *stationary random fields*, where the material coefficient tensor $\sigma(x, \omega)$ depends on both space and a probability space but with translation-invariant statistics. The objective is to find electric and current fields $E(x, \omega)$ and $J(x, \omega) = \sigma(x, \omega)E(x, \omega)$ satisfying the Maxwell-type conditions:

$$\nabla \cdot J = 0, \qquad \nabla \times E = 0, \qquad \mathbb{E}[E(x, \omega)] = E,$$

for a given mean field E.

To handle the lack of classical differentiability, the analysis uses a weak formulation using Sobolev spaces of random variables. Derivatives are generalized via a translation operator T_x, leading to a variational problem in a Hilbert space H of zero-mean, curl-free random vector fields. This space is equipped with an inner product combining L^2 norms and gradients:

$$\langle f, g \rangle_H = \int_\Omega f(\omega)g(\omega) \, dP(\omega) + \sum_{i=1}^{d} \int_\Omega L_i f(\omega) L_i g(\omega) \, dP(\omega),$$

where L_i are measure-adapted differential operators.

The effective property tensor σ^* is computed from the expected current, and the existence and uniqueness of solutions to the variational problem are ensured by the Lax-Milgram theorem, under boundedness and coercivity of the associated bilinear form.

This framework provides a rigorous method to compute or bound effective material parameters and lays the foundation for further analysis using spectral methods.

4.4 Modeling Ice Algal Blooms and Nutrient Transport in Flowing Environments

Group Members: Shivani Prabala, Emma Weber, Amelia McCarthy, Rachel Wissenbach, and Minji Kang

Motivation: Ice algal blooms in brine channel networks contribute significantly to primary productivity in polar ecosystems. These microbial communities interact strongly with their environment, relying on nutrient availability while producing EPS that can influence salinity, heat transport, and even ice structure. Understanding this feedback requires integrating biological growth with environmental transport mechanisms.

To this end, we aim to:

- Simulate algae and EPS dynamics in a confined, flowing domain.

- Study how advection and diffusion shape microbial distributions.

- Understand the role of wall interactions and vertical light gradients.

- Ultimately, couple nutrient-algae growth models with fluid flow to capture mutual feedback.

Workup:Biological Growth Model We began by implementing a reaction-diffusion system based on Zhao et al. [3], modeling algae P and nutrient N concentrations:

$$\frac{\partial P}{\partial t} = rcP\frac{N}{k_1 + N} - dP + D_P \Delta P$$
$$\frac{\partial N}{\partial t} = I_{\text{in}} + sdP - cP\frac{N}{k_1 + N} + D_N \Delta N$$

Here, growth is nutrient-limited and balanced by death, recycling, and diffusion. This model was used to reproduce bloom development in static environments.

Advection-Diffusion-Reaction Transport Model

To incorporate physical transport, we introduced a 2D flow model simulating nutrient, algae, and EPS concentrations $N(x, y, t), A(x, y, t), E(x, y, t)$:

$$\frac{\partial N}{\partial t} = -u(y)\frac{\partial N}{\partial x} + D\nabla^2 N - \alpha\frac{\mu N A}{K + N}$$
$$\frac{\partial A}{\partial t} = -u(y)\frac{\partial A}{\partial x} + D_A(y)\nabla^2 A + \frac{\mu N A}{K + N} - rA$$
$$\frac{\partial E}{\partial t} = -u(y)\frac{\partial E}{\partial x} + D_E(y)\nabla^2 E + \beta A S(t) - \lambda_E E$$

where $S(t) = \frac{1}{1 + e^{-k_{\text{eps}}(t - t_0)}}$ models time-dependent EPS activation.
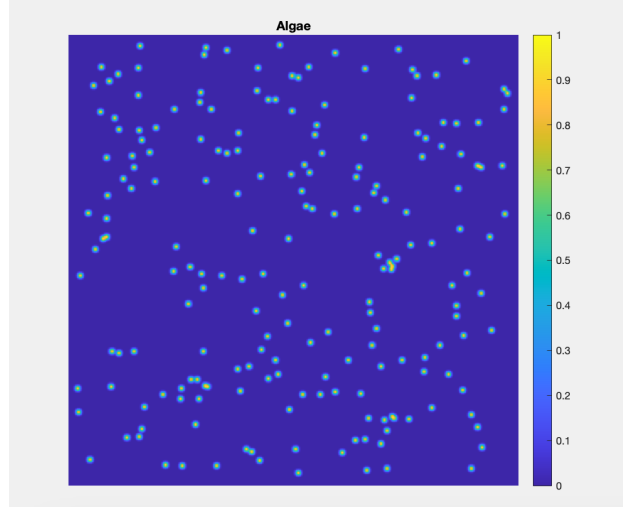
Figure 6: Simulation output from the algae-nutrient reaction-diffusion model based on Zhao et al. [3]. Nutrient uptake drives algal growth, while recycling from biomass death replenishes nutrients. Spatial diffusion leads to smooth concentration profiles, and the balance of growth and decay creates self-limiting bloom dynamics.

Flow Profile and Diffusivity   The velocity field $u(y)$ follows a parabolic laminar flow:

$$u(y) = u_{\max} \cdot \frac{4y(L_y - y)}{L_y^2}$$

Wall effects are captured using variable diffusivity:

$$D_A(y), D_E(y) \propto 1 - 0.5e^{-(y/\sigma)^2} - 0.5e^{-((L_y - y)/\sigma)^2}$$

Initial and Boundary Conditions   Fields are initialized using a Gaussian wall profile to promote realistic wall accumulation. Inflow boundary conditions introduce nutrients scaled by local velocity, while zero-gradient (Neumann) boundaries apply elsewhere.

Numerical Scheme   Simulations were performed on a 2D grid using forward Euler integration. Advection was handled via first-order upwind differencing, diffusion via a central Laplacian, and nonlinear source terms captured reaction dynamics. Results were visualized with dynamic contour plots.
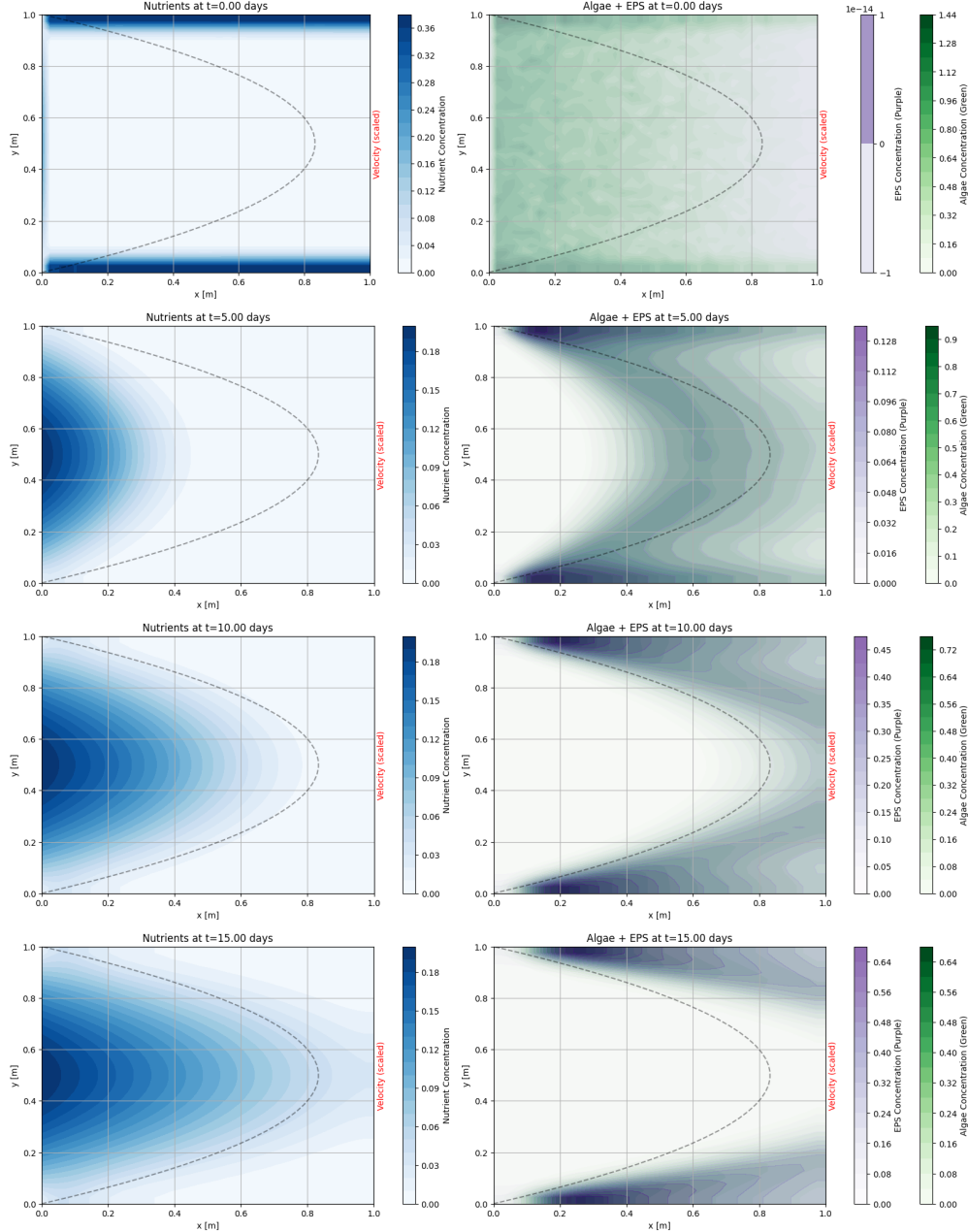
Figure 7: Contour plots of nutrient, algae, and EPS concentrations over time at $Pe = 10$. The results show flow-driven transport and bloom development.

Light Attenuation   To simulate vertical light limitations, we incorporated:

$$\text{light}(y) = \exp\left(-3\left(1 - \frac{y}{L_y}\right)^2\right)$$

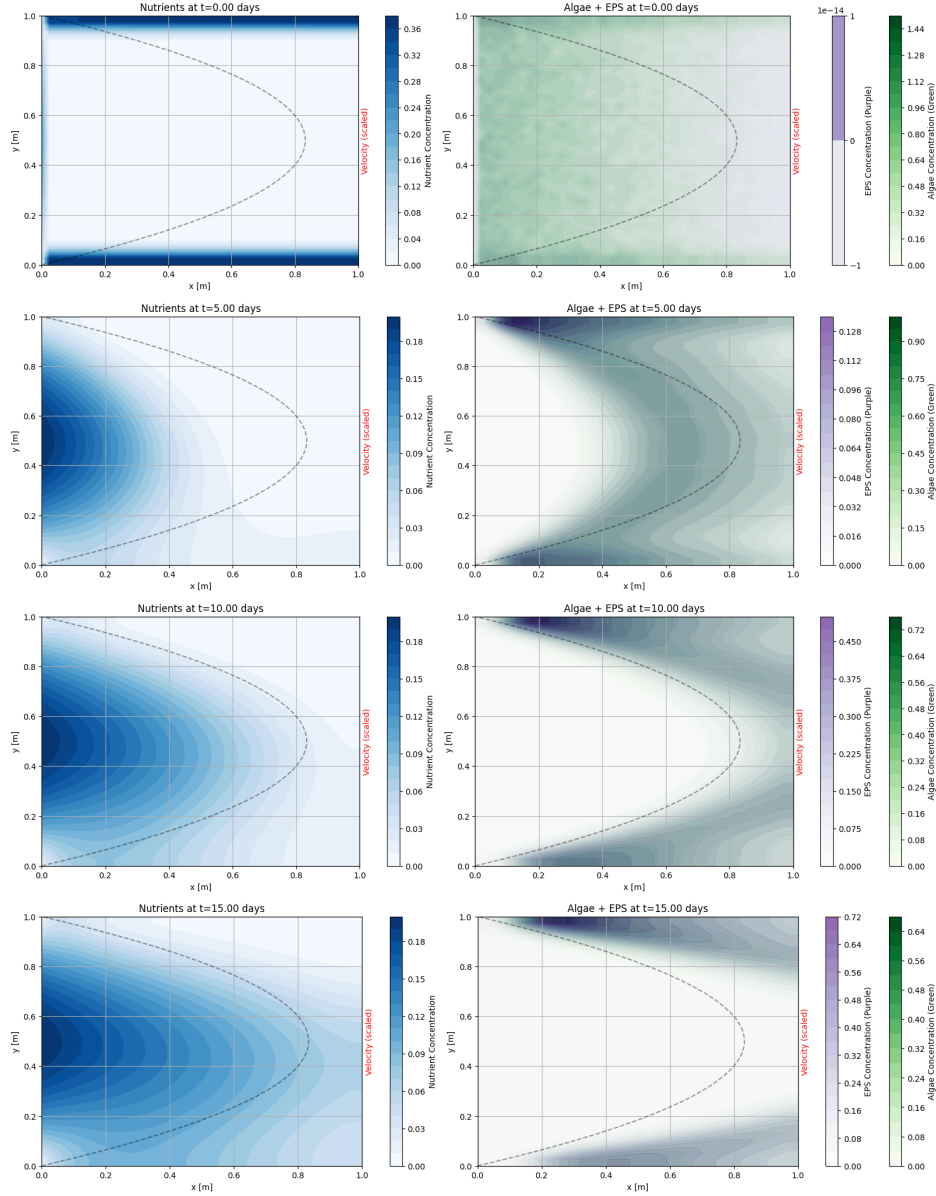This attenuated photosynthetic growth at depth by modifying the uptake term.

Figure 8: Simulation results at $Pe = 10$ including light attenuation effects. Algal growth is suppressed near the bottom due to reduced light availability, resulting in vertically stratified biomass and EPS distributions.

Simulation Results   Simulations at Péclet number $Pe = 10$ showed dynamic formation and downstream transport of algal blooms and EPS structures (Figure 7). Including light attenuation added vertical stratification with reduced growth near the bottom (Figure 8). EPS accumulation was suppressed near walls due to variable diffusivity, as observed in both cases.

Future Directions   Our goal was to fully couple the algae-nutrient growth model with the flow system to capture bio-physical feedbacks in dynamic sea ice environments. Key

extensions include:

- Modeling multiple brine channels to represent realistic sea ice porosity.

- Simulating EPS impacts on thermal and salinity fields.

- Transitioning to particle-based (discrete) models of algae and EPS.

- Parameter calibration and validation with observational data.

- Extending the system to 3D geometries.

EPS production is known to influence ice formation and brine structure, while flow and EPS together regulate nutrient availability. Coupling these systems will allow us to explore these interdependencies and improve the fidelity of biogeophysical sea ice models.

4.5   Water Wave Interactions with Sea Ice Media

Group members: Ian, Nicolas, Scott

Motivation: One of the key components affecting ice in the polar regions is its interaction with water waves. Of interest is a model that agrees with the observed amplitude attenuation and frequency of wave propagation as water waves interact with landfast ice and ice in the Marginal Ice Zone (MIZ).

Workup: The canonical model for wave propagation in the MIZ assumes that spectral wave energy obeys the equation

$$E(f, x) = E(f, x = 0)e^{-\alpha(f)x},$$

where f represents frequency, $x > 0$ denotes distance into the MIZ, and $\alpha(f)$ is the attenuation rate. It is typically assumed that the attenuation rate follows a power law, i.e. $\alpha(f) = cf^p$ for some constants $c, p > 0$. How might one model water wave interactions with the MIZ in order to recover such a relation? In hopes of building up to this goal, we briefly investigate water wave models in three separate scenarios: waves in open water, wave interactions with MIZ, and wave interactions with the MIZ.

One may model water waves in open water using Euler's equations along with other typically assumed conditions, such as incompressibility and seabed impermeability. For landfast ice, one may imagine a plate of ice covering the surface of the water for all $x > 0$, with free water for $x < 0$. Treating the ice as a thin plate and assuming different constitutive relations leads to different behaviors of the plate as it encounters incoming water waves. For example, one may model the plate as viscoplastic, meaning that it behaves as a solid until it reaches a certain threshold stress, after which the plate begins to behave as a fluid. One could then model the MIZ as an array of ice floes each separated by open water, like a "broken up" plate. Models become much more complicated at this point, and numerical approaches become much more appealing.

It has been determined in previous works that viscoplastic plate covers, as in the landfast ice scenario, do indeed lead to amplitude attenuation.

Future Directions: Future investigations include the numerical analysis of wave models in the MIZ, with an emphasis on determining which models agree with the typically assumed

(a) Seal Transition states

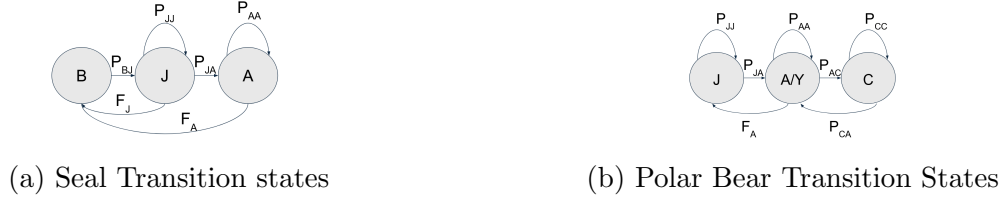(b) Polar Bear Transition States

Figure 9: Both stage-based models

spectral wave energy equation given above. As is always of interest in physical modeling, one may additionally seek a model that strikes a balance of simplicity and accuracy.

4.6 Coupled/Density Dependent Matrix Populations for Seals and Polar Bears

Group members: Rosie, Lilian, Victor, Jake, Amanda, Daniela, Garrett

4.6.1 Models and Setup

This presentation dealt with matrix models of polar bear and seal populations. First, we describe the models used. They are summarized in figure 9. The main ideas behind this presentation rely on transition matrices. These obey the equation

$$n_{t+1} = An_t$$

where A is the transition matrix, and n_t is the current population at time t. Using the fact that $n_{t+1} = A^t n_0$, and some linear algebra, we come across the fact that the long term behavior of the system will depend on the eigenvalues of A. In particular, if the largest eigenvalue is greater than 1, we expect the population to increase, and if is less than 1, it will decrease asymptotically.

The matrices we use for our states are

$$\begin{bmatrix} 0 & F_J & F_A \\ P_{BJ} & P_{JJ} & 0 \\ 0 & P_{JA} & P_{AA} \end{bmatrix}$$

for the seals, and

$$\begin{bmatrix} P_{JJ} & F_A & 0 \\ P_{JA} & P_{AA} & P_{CA} \\ 0 & P_{AC} & P_{CC} \end{bmatrix}$$

for the bears. Here, F_i is the fecundity of stage i, and P_{ij} is the probability of passing from stage i to j. Aligning with these matrices are our state vectors, where the number of seals is $S = \begin{bmatrix} S_B & S_J & S_A \end{bmatrix}^T$ and the bears are $B = \begin{bmatrix} B_J & B_A & B_C \end{bmatrix}^T$.

4.6.2   Coupling

For the probabilities themselves, we wanted to introduce coupling into the system, and so we introduced predation of seals by bears. Thus, the original probability of seals surviving must be augmented by the probability they are eaten. If $\hat{P}$ is a probability from the original, uncoupled model, and P_i^{NE} is the probability of a seal being eaten at stage i, we have our new probabilities as

$$P_{ij} = \hat{P}_{ij} P_i^{NE}.$$

For our coupling, we modeled the possibility of being eaten as

$$P_i^{NE} = 1 - \frac{1}{1 + exp\left(-\alpha\left(\frac{B_{tot}}{S_i} - 1\right)\right)}.$$

Here, B_{tot} is the total amount of bears. On the other hand, for the bears, the new probabilities are governed by the equations

$$P_B^A = 1 - \beta/S_{tot}$$
$$P_{ij} = P_{ij} P_B^A.$$

This gives us the new coupled transition matrices

$$\begin{bmatrix} 0 & F_J & F_A \\ P_{BJ}P_{S_B}^{NE} & P_{JJ}P_{S_J}^{NE} & 0 \\ 0 & P_{JA}P_{S_J}^{NE} & P_{AA}P_{S_A}^{NE} \end{bmatrix}$$

for the seals, and

$$\begin{bmatrix} P_{JJ}P_B^A & F_A P_B^A & 0 \\ P_{JA}P_B^A & P_{AA}P_B^A & P_{CA}P_B^A \\ 0 & P_{AC}P_B^A & P_{CC}P_B^A \end{bmatrix}$$

for the bears.

4.6.3   Results

We present our results here. The figures 10 show the total population of seals and bears. The figures 11 break down these populations into the various stages. Finally, figures 12 show the maximal eigenvalue at each time. Of particular note is the decline followed by recovery of bears. This change in behavior is mirrored in the eigenvalue charts.

4.6.4   Future Directions

Main ideas for the future include updating our models, by including more stages for each animal, updating the various probabilities used, or looking at environmental factors.

Another avenue is to look at the underlying linear algebra more. We could analyze the eigenvalues when the system is frozen in time, and find out what they are as functions of the parameters to perhaps investigate tipping point behavior.
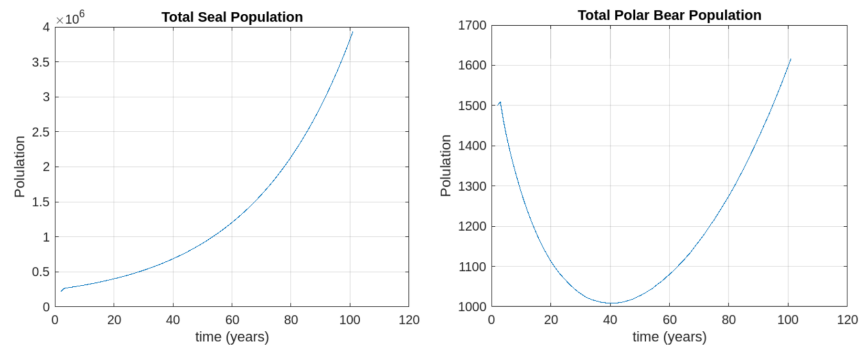
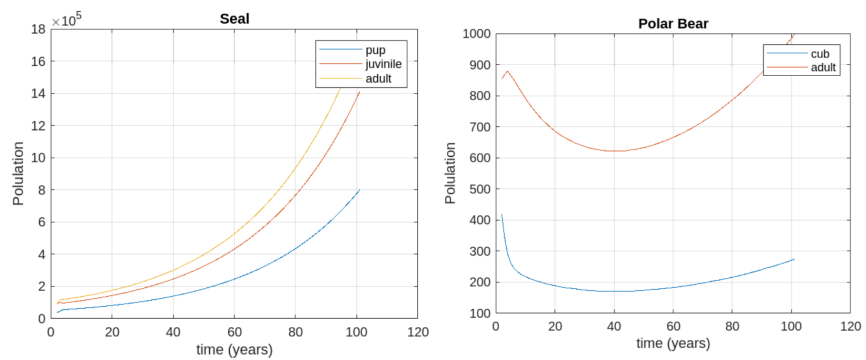Figure 10: Total Populations

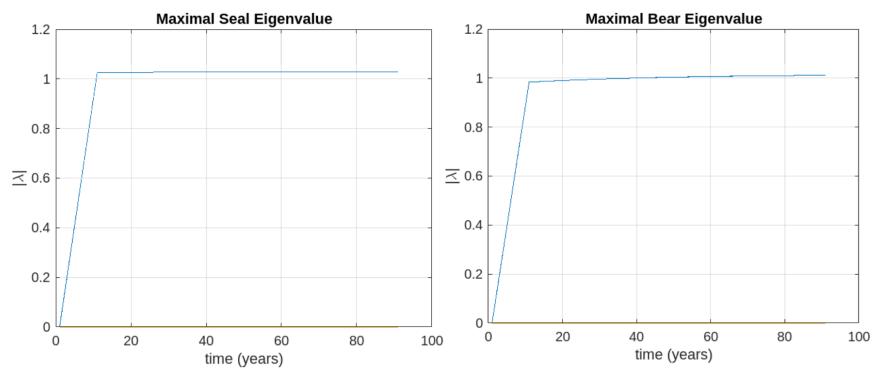
Figure 11: Stage Populations

Figure 12: Total Populations

4.7   Sobol' Indices of MPM Models

Group members: Ben, Abby

   Motivation: Matrix population models are highly interpretable and valuable tools for assessing population dynamics. The dominant eigenvalue of the matrix is a straightforward indicator of the health of the population in question. However, research exploring how uncertainty in the model inputs propagates to influence this dominant eigenvalue remains limited. Sobol' indices offer a rigorous framework to quantify the uncertainty of these models.

   Workup: Output variable Y can be considered as some function of input variables

$$Y = f(X_1, X_2, ..., X_k) = f_0 + \sum_i f_i + \sum_{i<j} f_{ij} + ... + f_{12...k}$$

where $f_{ij} = f(X_i, X_j)$ and the input variables are random variables. Through careful manipulation, the variance that the $f(X_i)$ function contributes to the total variance of the output can be calculated. This Sobol' index S_i is

$$S_i = \frac{V(E[Y|X_i])}{V(Y)}$$

Similar calculations are possible for higher order terms. Alternatively, for an X_i, the sum of its first order and higher order effects give indications of it's overall effect on the output variable. These total effect Sobol' indices S_{Ti} are also useful. For example, when $Y = f(X_1, X_2, X_3)$,

$$S_{T1} = S_1 + S_{12} + S_{13} + S_{123}$$

Our work applied Sobol' indices to a ringed seal MPM [2] to better understand the uncertainty apportionment. For instance, we were able to support the claim that the most important factor for continued population success is adult survival rate.

   Future Directions: We hope to apply these uncertainty apportionment techniques more broadly to matrix population models, with the goal of deepening our theoretical insight into MPMs and expanding the scope and rigor of research in this area.

4.8   SA/UQ of NPZ Models

Group members: Jenny, Mpho
Motivation:
Three-compartment nutrient–phytoplankton–zooplankton (NPZ) models are valued for their simplicity, yet their ability to capture real marine-ecosystem dynamics is contested. A rigorous, parameter-sensitivity study is therefore needed to judge when such minimalist frameworks remain suitable and when they should be replaced by more complex formulations.

Workup:
Truscott–Brindley PZ model

$$\frac{dP}{dt} = rP\left(1 - \frac{P}{K}\right) - \frac{R_m Z P^2}{\alpha^2 + P^2}, \qquad \frac{dZ}{dt} = \gamma R_m Z \frac{P^2}{\alpha^2 + P^2} - \mu Z$$

Busenberg–Kumar NPZ model

$$\frac{dP}{dt} = aP\frac{N}{k+N} - b\big(1 - e^{-cP}\big)Z - rP,$$

$$\frac{dZ}{dt} = Z\big[\delta\big(1 - e^{-cP}\big) - \varepsilon\big],$$

$$\frac{dN}{dt} = -aP\frac{N}{k+N} + rP + \varepsilon Z + \delta_1\big(1 - e^{-cP}\big)Z$$

Conservative two-equation reduction

$$\frac{dP}{dt} = aP\frac{N_T - P - Z}{k + N_T - P - Z} - b\big(1 - e^{-cP}\big)Z - rP, \qquad \frac{dZ}{dt} = Z\big[\delta\big(1 - e^{-cP}\big) - \varepsilon\big]$$

Each system was simulated with all biological parameters drawn from normal distributions having a 10% standard deviation around their baseline values; trajectories were analysed to identify the parameters that most strongly drive divergent behaviours.

Future Direction
Future work, we hope to widen the parameter ranges, test alternative sampling distributions, compute Sobol sensitivity indices to rank parameter influence quantitatively, and establish analytical links between the three formulations to explain why specific parameters dominate each model's dynamics.

5 Conclusions

The workshop successfully introduced multiscale modeling of polar systems and engaged students with hands-on tools for Arctic research. It positioned participants to contribute to pressing climate science challenges with mathematical tools.

A   Workshop Schedule and Participant List

B   Slides and Worksheets

Links to presentation slides, full worksheets, and coding notebooks.

Fractals Worksheet

Fractal geometry offers an elegant generalization of spatial dimension. Determining the spatial dimensions of common mathematical items, such as a line, square, sphere, or any other platonic object, can be quickly determined by a simple glance. However, more complicated geometries such as the Koch snowflake or the coastline of Australia have non-integer dimensions 1.262 and 1.13, respectively. One way of understanding this counter intuitive notion of non-integer dimension lies in how the mass of an object changes as it is scaled in size.

Let $M(L)$ denote the measure of an object relative to a characteristic length L. The value $M(L)$ is simply a measure of length, area, volume, or mass depending on the context of which dimension we are operating in. If a line of length 1 is scaled by a factor L, then its new measure is L, i.e., $M(1) = 1$ and $M(L) = L$. Similarly, the measure of a unit square satisfies the relation $M(L) = L^2$, and a unit cube satisfies $M(L) = L^3$. In fractal geometry, the power law that an object follows when subject to scaling (over a range of length scales L) determines its fractal dimension, i.e.,

$$M(L) \sim L^{D_f}. \tag{23}$$

Figure 13: Iterative construction of the Menger sponge, a three-dimensional generalization of the Cantor set.

Problem 1: Menger Sponge

Three iterations of the Menger sponge are shown in Figure 13.

1. Consider the first iteration of the Menger sponge shown in Figure 1. If this were to be shrunk by a factor of 3, how would you be able to construct the second iteration using

copies of this smaller, first iteration as building blocks? You can perform this same exercise for the second and third iterations shown in Figure 1 as well.

2. Suppose that $M(1) = 1$ for the complete Menger sponge. Compute $M(3)$ using the insight from part (a) and express your answer as a power of 3. Since this scaling law holds across all scales L, find D_f in the expression $M(L) = L^{D_f}$.

Problem 2

In fractal porous media, the number of pores with size greater than or equal to λ follows the scaling law

$$N(L \geq \lambda) = \left(\frac{\lambda_{\max}}{\lambda}\right)^{D_f} \tag{24}$$

where $\lambda_{\max}$ is the size of the largest pore. Equation 24 can also be applied to the number of islands on Earth.

For a porous material with $\lambda_{\max} = 9\text{mm}$ and $D_f = 1.7$ compute the following:

1. Number of pores of size $\geq 3\text{mm}$.

2. Number of pores of size $\geq 1\text{mm}$.

3. What happens as $\lambda \to 0$? Does this make sense for natural fractals or mathematical fractals?

4. Write the scaling law for the total number of pores for a fractal porous medium.

Problem 3

We can now draw an interesting connection between the number of pores and the total area of those pores (we are considering a 2D embedding, for simplicity). Consider the zeroth and first iterations of the Sierpinski carpet in Figure 2. Interpreting this as a porous medium, we consider the white squares to be pores and the dark squares to be solid.

1. Calculate the total area A_t of the porous medium by letting the side length be 3 units (This is specific for Figure 2(a). The side length can be considered to be 9 in Figure 2(b)). Write your answer as a scaling law similar to Equation (24) and specify what $\lambda_{\max}$ and $\lambda_{\min}$ are. Here, $\lambda_{\max}$ and $\lambda_{\min}$ can be interpreted as the upper and lower limits of self-similar regions, respectively.

2. Compute the area of pores A_p in Figure 2 and express this as a scaling law similar to part (a), but now with a different scaling exponent. What do you notice about this exponent?

3. The porosity ϕ can be computed as the ratio A_p/A_t. Write out the scaling law for porosity ϕ, then find an expression for the fractal dimension D_f.

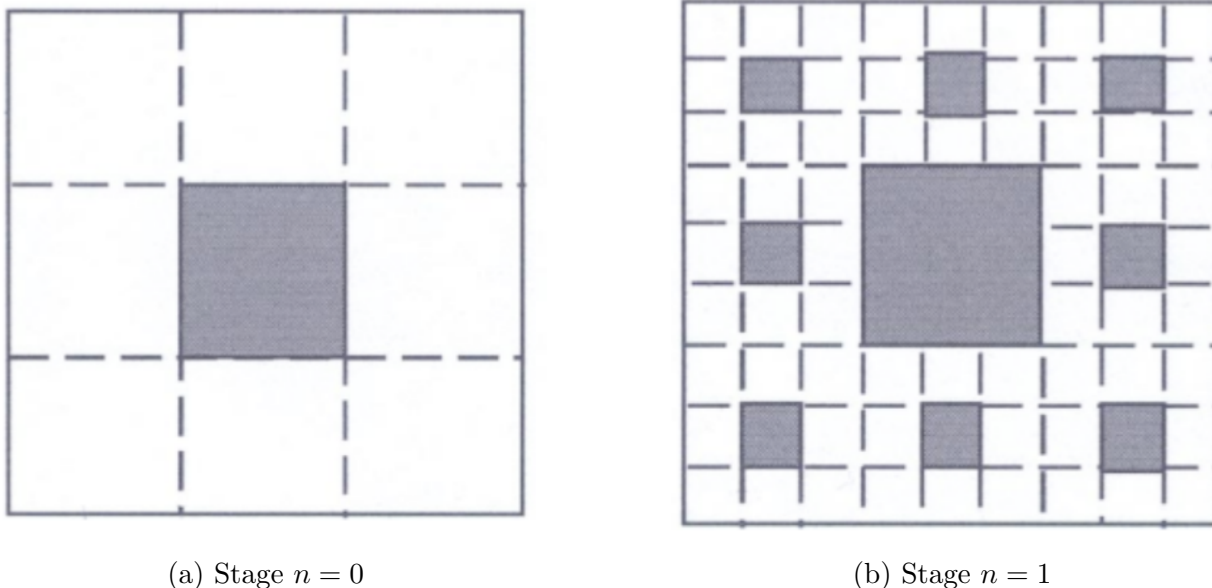4. Verify that your equation for D_f works when plugging in suitable values derived from Figure 14.

(a) Stage $n = 0$ (b) Stage $n = 1$

Figure 14: Sierpinski carpets of (a) stage $n = 0$ and (b) stage $n = 1$.

Diffusion and Sea Ice Worksheet

Activity #1: Diffusion via random walks

Consider a sequence of independent and identically distributed random variables,

$$Y_1, Y_2, ..., Y_n, ...,$$

representing random jumps made by a particle. For the time being, we will assume that these jumps occur on the x-axis ($\mathbb{R}$), and we will require only that (i) the probability density function (pdf) describing the lengths of the jumps x, denoted $f(x)$, exists, and (ii) all moments $\mathbb{E}[Y_i^k] < +\infty$ for each $i \in \mathbb{N}$. Moreover, define $\mathbb{E}[Y_i] = \mu_1$ and $\mathbb{E}[Y_i^2] = \mu_2$. By "moments", we mean

$$\mathbb{E}[Y_i^n] := \int_{-\infty}^{\infty} x^n f(x) dx. \tag{25}$$

In a simple case, the pdf could simply give a one-half probability of a jump to the left and a one-half probability of a jump to the right.

We will define a random walk as the sum of many such jumps,

$$S_n = \sum_{i=1}^{n} Y_i,$$

and aim to connect this random walk to the diffusion equation. One of our main tools toward this goal will be the Fourier transform; while there are other excellent ways to connect

diffusion and random walks, the one that we will follow here has the natural advantage of also being applicable to the study of so-called *anomalous* diffusion.

There are a few different conventions for the Fourier transform. Here, we will use

$$\hat{g}(k) := \int_{-\infty}^{\infty} g(x)e^{-ikx}dx,$$

where $\hat{g}(k)$ will denote the Fourier transform of an arbitrary function, g. (For reference, we will also define the inverse Fourier transform, which relates the original function, $g(x)$, to its Fourier transform $\hat{g}(k)$:

$$g(x) := \frac{1}{2\pi} \int_{-\infty}^{\infty} \hat{g}(k)e^{ikx}dk.$$

Using a Taylor expansion, show that the Fourier transform of the pdf $f(x)$ is

$$\hat{f}(k) = 1 - (ik)\mu_1 - \frac{k^2}{2}\mu_2 + o(k^2), \tag{26}$$

where, as a reminder, $f(x)$ is the pdf of each of the jumps, Y_i. Using the independence of the jumps Y_i, show that the n-step random walk S_n has Fourier transform $\left(\hat{f}(k)\right)^n$. (**Hint:** an especially "clean" way to do this involves realizing that $\hat{f}(k) = \mathbb{E}[e^{-ikY_i}]$ for each Y_i! You may also need the property that $\mathbb{E}[XY] = \mathbb{E}[X]\mathbb{E}[Y]$ when random variables X and Y are independent. Also note that you never actually need to compute any of the Fourier transforms; an appropriate Taylor expansion is enough!)

Using a similar argument and supposing (for simplicity) that $\mu_1 = 0$ and $\mu_2 = 2$, show that the normalized sum $\frac{S_n}{\sqrt{n}}$ has Fourier transform

$$\left(\hat{f}(\frac{k}{\sqrt{n}})\right)^n = \left(1 - \frac{k^2}{n} + o(n^{-1})\right)^n.$$

In the limit as $n \to \infty$, the above Fourier transform becomes one of our very best friends (mathematically)! How do you evaluate this limit?

Now consider the *rescaled random walk* where we replace n by ct, where t represents time and c is whatever scaling factor we need. Show that $S_{[ct]}$ has a Fourier transform e^{-k^2t} using a lightly modified version of the argument made above.

It's nice to take a moment to think about what we've actually achieved through these formal manipulations: we have now shown that the Fourier transform of the normalized random walk's pdf is e^{-k^2t}, regardless of the *underlying jump distribution*[2], which gets us *very close*

---

[2]At least, under some very mild conditions on the pdf of the jumps.

to understanding the underlying random walk's pdf. Having obtained *Fourier transform* of the pdf, it is very natural to ask next: *but what is the actual pdf?*

Show, via table-lookup if you like, that the inverse Fourier transform of $e^{-k^2 t}$ is

$$p(x,t) := \frac{1}{\sqrt{4\pi t}} e^{-\frac{x^2}{4t}},$$

which is the pdf of the normalized random walk $n^{-1/2} S_{[ct]}$.

Next, argue that $\hat{p}(k,t)$ solves the ODE

$$\frac{d\hat{p}}{dt} = -k^2 \hat{p} = (ik)\hat{p},$$

and that this ODE can be inverted to

$$\frac{\partial p}{\partial t} = \frac{\partial^2 p}{\partial x^2}. \tag{27}$$

This shows that our rescaled random walk, in the long-time (or, equivalently, "many jumps") limit, has a pdf that satisfies a normal distribution. Remarkably, that same pdf satisfies the diffusion equation![3]

Optional— a hypothetical: Suppose that we had instead obtained a $\hat{p}(k,t)$ satisfying

$$\frac{d\hat{p}}{dt} = (ik)^{\alpha/2}\hat{p}.$$

What PDE would this be associated with upon inversion of the Fourier transform? It turns out that the argument we followed above can be revisited in a slightly generalized way to the case that the jump distribution *does not* have all of its moments— for example, consider a certain Pareto distribution, whose pdf is

$$f(x) = \frac{\alpha}{x^{\alpha+1}} \tag{28}$$

on $x \in [1,\infty)$. Which moments exist for the Pareto distribution? Where does the argument we followed above fail?[4]

---

[3]We have brushed any discussion of the domain of solution or the boundary conditions "under the rug"; as an **extra challenge**, consider what sort of domain and "boundary conditions" would be appropriate here so that our solution is preserved. *It may be worth noticing that "boundary conditions" are in quotes here.*

[4]In fact, this line of inquiry leads directly to the idea of *anomalous diffusion*; the Pareto distribution means, in some sense, that the particle in question is capable of "long jumps".

Activity #2: Pipe bounds on the effective permeability

We restrict our consideration of the brine pore space to the much simplified case that all pores are shaped like small, cylindrical pipes arranged in parallel, each having the same radius a. The Stokes equations reduce to

$$\frac{1}{r}\frac{\partial}{\partial r}\left(r\frac{\partial w}{\partial r}\right) = -1, \quad r < a$$
$$w = 0, \quad r = a$$
$$w < \infty, \quad r = 0$$

$$(29)$$

after an appropriate change of coordinates. In this geometry, we are only interested in the z-aligned component of the effective permeability tensor, k_{zz}. Solve for w, the z-component of the velocity field, from the above equations. Then argue that the effective permeability of one cylindrical pipe, of the kind described above, is simply the average velocity w through the pipe. Finally, argue that the effective permeability k of a porous medium consisting of ϕ brine fraction and a cylindrical pipe-like microstructure is

$$k = \frac{\phi a^2}{8}.$$

$$(30)$$

This effective permeability is the so-called *pipe bound* for a specified radius a.

Before proceeding, consider the effect of supposing that all of the randomly-placed brine pores look like small, parallel pipes aligned in the same direction. This scenario is, in some sense, "extreme". Should it lead to an *overestimate* or an *underestimate* of the effective permeability for random porous media where all pore geometries (and orientations) are allowed? *Debate and discuss as vigorously as you like, but please remember that if you break furniture, we lose our security deposit.*

If, above, you concluded that the "parallel cylinders" provide an overestimate of the effective permeability, consider what pore geometry and orientation might be associated with an underestimate. If, instead, you concluded that the "parallel cylinders" provide an underestimate, then consider what pore geometry and orientation might be associated with an overestimate. This doesn't need to be fully rigorous; a heuristic approach is just fine. *You may also want to be on the lookout for an interesting analogy between these estimates and certain bounds that may arise in the homogenization session for a completely different physical context.*

Variable radius a. The above simplification is, unsurprisingly, a little too simple. Perovich and Gow (1996) and Bock and Eicken (2005) show that the average cross-sectional area of a pore increases substantially with temperature and brine volume fraction ϕ. An empirical approximation leads to

$$k = \frac{\phi[a(\phi)]^2}{8}.$$

$$(31)$$

where $a(\phi) = 7 \times 10^{-5} + (1.6 \times 10^{-4})\phi$ in units of meters. In Figure 15, we compare experimental data with the pipe bound, Equation (31). It is clear that the agreement is excellent: the experimental data do, indeed, respect the theoretical bound!
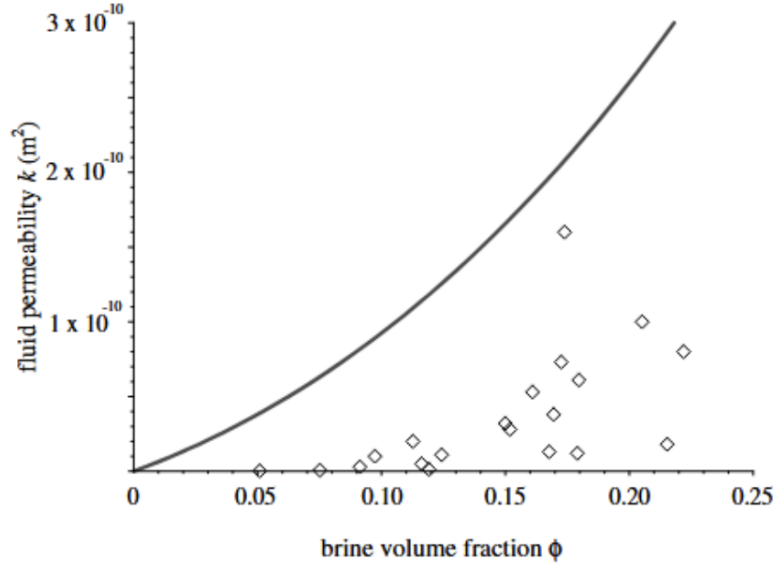

Figure 15: The void upper bound in Equation (31) is represented by the curve above. It captures laboratory data on the vertical fluid permeability of artificially grown sea ice, represented by the diamonds. This figure is adapted from Figure 3 of Golden et al., Void bounds for fluid transport in sea ice, *Mechanics of Materials*, 38, pp. 801-817, 2006.

Activity #3: Advection-enhanced diffusion

Here, we will consider the advection-diffusion equation,

$$\frac{\partial \theta}{\partial t} + \vec{u} \cdot \nabla \theta = \kappa \nabla^2 \theta, \tag{32}$$

where $\theta(x, y, t)$ is the density of some particles ("tracers") that are advected by a background velocity field $\vec{u}(x, y, t)$ and experience molecular diffusion with diffusion coefficient κ. By *advection-enhanced diffusion*, we mean that the diffusion of an initial tracer profile is enhanced by the presence of the background velocity field $\vec{u}$.

If this sounds a little strange, don't worry: you've almost certainly exploited this phenomenon before in your everyday life. If you have ever

- jiggled a tea bag in a hot cup of water to make your tea brew faster,

- mixed a protein shake with a spoon, or

- swirled creamer into a coffee,

you have exploited the phenomenon of advection-enhanced diffusion (good job!) by inducing a velocity field that causes the solution to mix faster than it would have if you had just left it alone.

Enhancement of diffusion by shear flow. For simplicity, we will consider the classic example of Equation (32) in an infinitely-long, cylindrical channel of radius a. A schematic is shown in Figure 16.

First, convert Equation (32) to cylindrical coordinates under the assumption of symmetry about the axis of the pipe. Hence only two variables, x, the location along the axis of the pipe, and r, the radial coordinate, are needed. Show that Equation (32) reduces to

$$\frac{\partial \theta}{\partial t} + u(r)\frac{\partial \theta}{\partial x} = \kappa\left(\frac{\partial^2 \theta}{\partial x^2} + \frac{1}{r}\frac{\partial}{\partial r}\left(r\frac{\partial \theta}{\partial r}\right)\right) \tag{33}$$
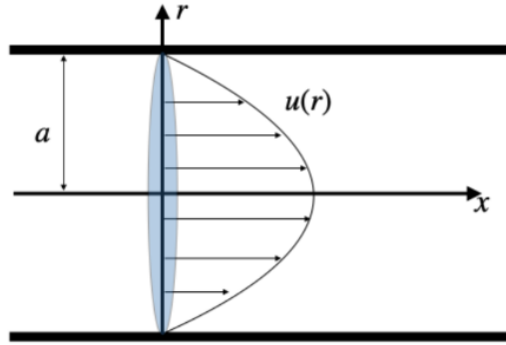

Figure 16: A schematic of shear flow in an axisymmetric pipe.

Consider the *shear flow*,

$$u(r) = 2\bar{u}\left(1 - \frac{r^2}{a^2}\right)$$

where $\bar{u} = \frac{2}{a^2}\int_0^a urdr$. Observe that $\frac{\partial \bar{u}}{\partial r} = 0$; this fact will be useful later.

Now consider the decompositions

$$\theta(x, r, t) = \bar{\theta}(x, t) + \theta'(x, r, t)$$
$$u(x, r) = \bar{u}(x) + u'(x, r), \tag{34}$$

where $\bar{\theta} = \frac{2}{a^2}\int_0^a \theta rdr$, and $\bar{\theta}' = 0$. *Before proceeding, consider what physical assumptions are being made.*

Apply the above decompositions to Equation (33), simplifying where possible. Take the average of the resulting equation across the radius r and conclude that

$$\partial_t \bar\theta + \bar u \partial_x \bar\theta + \overline{u' \partial_x \theta'} = \kappa \partial_x^2 \bar\theta. \tag{35}$$

At this point, we have an equation that is *almost* entirely in terms of averaged quantities $\bar\theta$ and $\bar u$, except for an annoying $\overline{u' \partial_x \theta'}$! Eliminating this term is our next order of business.

To this end, we make a strategic change of coordinates,

$$\xi = x - \bar u t, \tau = t. \tag{36}$$

Show that this change of coordinates leads to

$$\partial_\tau(\bar\theta + \theta') + u' \partial_\xi(\bar\theta + \theta') = \kappa \left(\frac{1}{r} \partial_r \big(r \partial_r \theta' \big) \right); \tag{37}$$

or, if you're running out of time, feel free to accept it as a "fact".

At this point, several physical assumptions are made which relate to the slow variation of $\bar\theta, \theta'$; that $\bar\theta \gg \theta'$; and that a "long time" has elapsed, so that $\partial_\tau \theta'$ can be neglected. We also assume that $\bar\theta, \theta', \bar u$ and u' are sufficiently smooth as to allow as many derivatives as we need. **We neglect these details here for brevity, but invite you to chase them down later as an extra challenge**!

The equation derived above can be shown to reduce to

$$u' \partial_\xi \bar\theta = \kappa \left(\frac{1}{r} \partial_r \big(r \partial_r \theta' \big) \right). \tag{38}$$

Show that this leads to

$$\theta' = \frac{\bar u \partial_\xi \bar\theta}{\kappa} \left(\frac{r^2}{4} - \frac{r^4}{8a^2} + A \ln(r) + B \right),$$

where A, B are constants that can be determined from boundary and regularity conditions... and determine them!

Returning to x, r coordinates, and having obtained θ', we can now compute $\overline{u' \partial_x \theta'}$. Then, substituting, we obtain

$$\partial_t \bar\theta + \bar u \partial_x \bar\theta = \left(\kappa + \frac{a^2 \bar u^2}{48\kappa} \right) \partial_x^2 \bar\theta, \tag{39}$$

which is simply an advection-diffusion equation in the averaged tracer density $\bar\theta$. Hence we may identify

$$\kappa_{\text{eff}} = \left(\kappa + \frac{a^2 \bar u^2}{48\kappa} \right). \tag{40}$$

This shows that the presence of shear flow "enhances" the effective diffusion!

C References and Resources

[1] Paul E. O'Keeffe and Sebastian Wieczorek. Tipping phenomena and points of no return in ecosystems: Beyond classical bifurcations, 2020.

[2] Jody R Reimer, Hal Caswell, Andrew E Derocher, and Mark A Lewis. Ringed seal demography in a changing climate. *Ecological Applications*, 29(3):e01855, 2019.

[3] Li-Xia Zhao, Kang Zhang, Koen Siteur, Xiu-Zhen Li, Quan-Xing Liu, and Johan van de Koppel. Fairy circles reveal the resilience of self-organized salt marshes. *Science Advances*, 7(6):eabe1100, 2021.